

STUDY OF CREEP OF ALUMINA-FORMING AUSTENITIC STAINLESS STEEL  
FOR HIGH-TEMPERATURE ENERGY APPLICATIONS

A Thesis  
Submitted to the Faculty  
in partial fulfillment of the requirements for the  
degree of  
Master of Science  
by

NATALIE PETROVNA AFONINA

Thayer School of Engineering  
Dartmouth College  
Hanover, New Hampshire  
22 November, 2016

Examining Committee:

Chairman \_\_\_\_\_  
(Dr. Ian Baker)  
Member \_\_\_\_\_  
(Dr. Harold Frost)  
Member \_\_\_\_\_  
(Dr. Rachel Obbard)

---

F. Jon Kull  
Dean of Graduate and Advanced Studies



## ABSTRACT

To withstand the high temperature ( $>700^{\circ}\text{C}$ ) and pressure demands of steam turbines and boilers used for energy applications, metal alloys must be economically viable and have the necessary material properties, such as high-temperature creep strength, oxidation and corrosion resistance, to withstand such conditions. One promising class of alloys potentially capable of withstanding the rigors of aggressive environments, are alumina-forming austenitic stainless steels (AFAs) alloyed with aluminum to improve corrosion and oxidation resistance. The effect of aging on the microstructure, high temperature constant-stress creep behavior and mechanical properties of the AFA-type alloy Fe-20Cr-30Ni-2Nb-5Al (at.%) were investigated in this study.

The alloy's microstructural evolution with increased aging time was observed prior to creep testing. As aging time increased, the alloy exhibited increasing quantities of fine  $\text{Fe}_2\text{Nb}$  Laves phase dispersions, with a precipitate-free zone appearing in samples with higher aging times. The presence of the  $\text{L}1_2$  phase  $\gamma^{\prime}$ - $\text{Ni}_3\text{Al}$  precipitate was detected in the alloy's matrix at  $760^{\circ}\text{C}$ .

A constant-stress creep rig was designed, built and its operation validated. Constant-stress creep tests were performed at  $760^{\circ}\text{C}$  and 35MPa, and the effects of different aging conditions on creep rate were investigated. Specimens aged for 240 h exhibited the highest creep rate by a factor of 5, with the homogenized sample having the second highest rate. Samples aged for 2.4 h and 24 h exhibited similar low secondary

creep rates. Creep tests conducted at 700°C exhibited a significantly lower creep rate compared to those at 760°C.

Microstructural analysis was performed on crept samples to explore high temperature straining properties. The quantity and size of  $\text{Fe}_2\text{Nb}$  Laves phase and NiAl particles increased in the matrix and on grain boundaries with longer aging time.

High temperature tensile tests were performed and compared to room temperature results. The high temperature results were significantly lower when compared to room temperature values. Higher creep rates were correlated with lower yield strengths.

## ACKNOWLEDGEMENTS

I would like to thank:

My adviser Professor Ian Baker, whose patience, expertise, unwavering support and encouragement made it possible for me to complete my studies.

The Baker Lab Research Group for their support and guidance.

The Carpenter Technology Corporation for providing test material for this study.

Claire Stolz, for the pep talks worthy of rousing armies and accompanying me on moonlit Methow walks. Without you by my side the cougars would've gotten me.

Nate Beatty, for being there in the darkest hour, for sharing a love of micro-adventures, waking up at the crack of dawn for sunrise hikes, teaching me how to properly eat lobsters and always having my back.

Mark Fischer, for being a watchful older brother, being one of the few that understands what to do when you hear ‘hop hop hop!’ and lending a new perspective. You’ve kept me successfully out of trouble most of the time. I’m already looking forward to our next adventure.

Julian Childs-Walker, for being my twin and remaining the only person to ever hitchhike past the Arctic Circle to adventure with me. You’ve continuously helped me get up to no good and our conversations help me make sense of this world.

I can’t convey how much I owe my family for getting me this far.

My sister Jane Bellousov for being the level-headed one in the family and your incredible resilience. I can’t wait to go on more adventure trips with you as we grow older together.

My father Yevgeniy Belousov, for encouraging me to stop working so hard and go on more climbing breaks outside. You’ve provided much needed perspective and inspiration.

My grandmother Dr. Galina Gataulina for worrying about my academic timeline, encouraging me not to procrastinate and feeding me delicious piroshki.

My grandfather Dr. Akhiyar Myginovich for reminding me that life can be filled with meaningful work and to never lose your inner child wonder of how the world works. For always being proud and supportive and teaching me how to use a crowbar to pull nails and lay bricks in a straight line. You encouraged me on my path to graduate school, and I wish you'd still be here to see me complete what I started.

Most importantly, my mother Dr. Irina Afonina, without whom I would not be here today. Who supported me at every step from the moment the two of us immigrated to the United States from Russia. You gave me room to figure things out on my own and spread my wings. You sadly left us before I could finish this thesis, but I know you would've been proud of me and would have loved to do the first round of edits.

*I dedicate this thesis to my mother.*

*Your support, unconditional love and sacrifices are responsible for everything I've accomplished.*

## TABLE OF CONTENTS

Abstract	ii
Acknowledgements	iv
Table of Contents	vi
List of Tables	x
List of Figures	xi
Chapter 1 Introduction	1
1.1 Background	1
1.2 Alumina-Forming Austenitic Stainless Steels	3
1.3 AFA precipitates	4
1.4 Outline of Research Project	10
Chapter 2 Constant-Stress Creep Rig Design and Calibration	12
2.1 Introduction	12
2.2 Overview of Constant-Stress Creep Machines	12
2.3 Design of Creep Test Rig	15
2.3.1 Frame and Mounts	18
2.3.2 Constant-Stress Cam	18
2.3.3 Angular Displacement Transducer	20

2.3.4 Cable and Load Alignment	21
2.3.5 Specimen Grip Components	23
2.3.6 Making Adjustments	25
2.3.7 Data Logging	26
2.4 Testing and Verification	27
2.4.1 Identifying the ADT Adjustment Factor	27
2.4.2 Eliminating Creep Contributions From System Components	29
2.4.3 Furnace Temperature Profile	29
2.4.4 Calibration Testing	30
Chapter 3 Experimental Methods	32
3.1 Introduction	32
3.2 Materials Preparation	32
3.2.1 Materials Used	32
3.2.2 Sample Machining	33
3.2.3 Material Homogenization	34
3.2.4 Annealing	35
3.3 Materials Characterization	35
3.3.1 Scanning Electron Microscopy	35

3.3.2 Transmission Electron Microscopy	37
3.4 Constant-Stress Creep Testing	37
3.4.1 Sample Preparation	37
3.4.2 Creep Test Experimental Procedure	38
3.4.3 Creep Test Experiments Performed	40
3.5 Tensile Tests	41
Chapter 4 Effect of Aging Time on Microstructure and High Temperature Tensile and Constant-Stress Creep Behavior of the Alumina-Forming Austenitic Stainless Steel	44
4.1 Introduction	44
4.2 Experimental	44
4.3 Results and Discussion	46
4.3.1 Investigating presence of $\gamma'$ -Ni <sub>3</sub> Al (L12) precipitates at 760°C	46
4.3.2 Characterizing the effects of aging time on alloy's microstructure	47
4.3.3 Effect of aging time on high temperature tensile behavior	51
4.3.4 Effect of aging time on constant-stress creep properties	55
4.3.5 Effect of aging temperature on constant-stress creep rate	61
4.3.6 Effect of aging time on post-creep test microstructure	62
Chapter 5 Summary and Conclusions	73

Chapter 6 Future Work	77
Appendices	79
Appendix I: Constant-Stress Derivation	79
Appendix II: Custom CAD Files for Creep Rig	81
Appendix III: Additional high temperature constant-stress creep curves for each aging condition	88
Appendix IV: Additional high temperature tensile curves for each aging condition	90
References	92

## LIST OF TABLES

Table 2.1: Coordinates for the constant-stress cam profile fabricated for use in this study, with $a = 6.00$ in and $b = 0.95$ in.....	19
Table 3.1: Alloy compositions obtained by chemical quantitative analyses.....	33
Table 4.1: Area fraction of grain boundary (GB) Laves phase for Fe-20Cr-30Ni-2Nb-5Al (at. %) homogenized at $1250^{\circ}\text{C}$ and aged at $800^{\circ}\text{C}$ for 0, 2.4, 24 or 240 h with results from this investigation in the left column and results from Trotter et al. in the right column. GB area fractions are calculated from an average of at least three BSE images for each aging condition. .....	51
Table 4.2: Yield strength (YS), ultimate tensile strength (UTS), and elongation to failure ( $\varepsilon_f$ ) for Fe-20Cr-30Ni-2Nb-5Al (at. %) homogenized at $1250^{\circ}\text{C}$ for 24 h, heat treated at $800^{\circ}\text{C}$ and strained under tension at $760^{\circ}\text{C}$ or at room temperature with an initial strain rate of $5 \times 10^{-4} \text{ s}^{-1}$ . Results are the average of at least three tests at each condition.....	53
Table 4.3: Values prior to creep and after creep testing of average particle diameter and particle density for Fe-20Cr-30Ni-2Nb-5Al (at. %) homogenized at $1250^{\circ}\text{C}$ for 24 h, then subsequently aged at $800^{\circ}\text{C}$ for 2.4, 24 or 240 h and crept at $760^{\circ}\text{C}$ for 500 h under a load of 35 MPa in air.....	65
Table 4.4: Volume fraction and standard deviations for NiAl and Laves phase particles for Fe-20Cr-30Ni-2Nb-5Al (at. %) homogenized at $1250^{\circ}\text{C}$ for 24 h and aged at $800^{\circ}\text{C}$ . Creep testing was conducted at $760^{\circ}\text{C}$ for 500 h under a load of 35 MPa in air.....	68

Table 4.5: Post-creep T-bone head and gauge comparison values of average Laves phase and NiAl particle diameter and particle density for Fe-20Cr-30Ni-2Nb-5Al (at. %) homogenized at 1250°C for 24 h and aged at 800°C for 240 h. Creep testing was conducted at 760°C for 500 h under a load of 35 MPa in air.....71

## LIST OF FIGURES

Figure 1.1: Diagram of the L1 <sub>2</sub> -ordered $\gamma'$ -Ni <sub>3</sub> Al precipitate crystal structure.....	6
Figure 1.2: Diagram of the hexagonal C14 Fe <sub>2</sub> Nb Laves phase structure.....	7
Figure 1.3: Backscattered electron images showing Fe <sub>2</sub> Nb Laves phase (light contrast) and B2-type NiAl phase (dark contrast) precipitates in the matrix of Fe-20Cr-30Ni-2Nb- 5Al (at. %) homogenized at 1250°C and heat-treated at 800°C for 240 h.....	9
Figure 2.1: A schematic diagram detailing a weight-transferring system used for constant- stress creep tests.....	13
Figure 2.2: A diagram detailing the coordinate system used for the cam profile.....	14
Figure 2.3: Photograph of the constant-stress creep machine with system components labeled matching the key.....	16
Figure 2.4: Design drawing of constant-stress cam.....	22
Figure 2.5: Diagram of specimen grips.....	24
Figure 2.6: Plot of the constant-stress cam geometry. The cam's centerline is centered on $y = 0$ .....	26
Figure 2.7: Plot of system displacement measurements taken with ADT, manually with a micrometer and the same ADT results plotted with an adjustment factor. Notice the adjusted ADT measurements match those taken with the micrometer.....	28
Figure 2.8: Load calibration of constant-stress cam .....	31
Figure 3.1: CAD file drawing of a T-bone specimen inserted into one side of the creep machine's specimen grips.....	34

Figure 3.2: Dimensions of creep test specimen in millimeters.....	37
Figure 3.3: Diagram detailing the locations of sections taken for SEM microstructural analysis from crept T-bones. (A) Gauge (B) Head (C) Gauge-lengthwise.....	39
Figure 3.4: Dimensions of tensile test specimen in millimeters.....	41
Figure 4.1: (a) Bright-field TEM image of Fe-20Cr-30Ni-2Nb-5Al (at. %) homogenized at 1250°C for 24 h, aged at 800°C for 24 h and crept for ~800 h at 760°C with an arrow indicating the matrix; (b) corresponding selected area diffraction pattern of the matrix showing $\gamma'$ -Ni <sub>3</sub> Al (L1 <sub>2</sub> ) superlattice reflections (arrowed).....	47
Figure 4.2: BSE SEM images of Fe-20Cr-30Ni-2Nb-5Al (at. %) homogenized at 1250°C for 24 h (a), then subsequently aged at 800°C for 2.4 h (b), 24 h (c), and 240 h (d). The light precipitates are the Laves phase.....	49
Figure 4.3: High temperature tensile curves of Fe-20Cr-30Ni-2Nb-5Al (at. %) homogenized at 1250°C for 24 h and subsequently aged at 800°C for 0, 2.4, 24 or 240 h as indicated. Tensile tests were conducted at 760°C with an initial strain rate of $5 \times 10^{-4} \text{ s}^{-1}$ . Results are the average of at least three tests at each condition.....	52
Figure 4.4: BSE image of fracture surface for Fe-20Cr-30Ni-2Nb-5Al (at. %) after being homogenized at 1250°C for 24 h, aged at 800°C for 240 h and strained under tension at 760°C with an initial strain rate of $5 \times 10^{-4} \text{ s}^{-1}$ .....	55
Figure 4.5: Initial five hours of constant-stress creep curves for Fe-20Cr-30Ni-2Nb-5Al (at. %) conducted at 760°C under a 35 MPa load in air. Specimens were homogenized at	

1250°C for 24 h and subsequently aged at 800°C for 0, 2.4, 24 or 240 h prior to creep testing. Two creep tests were performed for each aging protocol.....	56
Figure 4.6: Constant-stress creep curves for Fe-20Cr-30Ni-2Nb-5Al (at. %) conducted at 760°C for 500 h under a 35 MPa load in air. Specimens were homogenized at 1250°C for 24 h and subsequently aged at 800°C for 0, 2.4, 24 or 240 h prior to creep testing. Two creep tests were performed for each aging protocol.....	57
Figure 4.7: Strain rate as a function of strain are plotted for Fe-20Cr-30Ni-2Nb-5Al (at. %) conducted at 760°C for 500 h under a 35 MPa load in air. Specimens were homogenized at 1250°C for 24 h and subsequently aged at 800°C for 0, 2.4, 24 or 240 h prior to creep testing.....	59
Figure 4.8: Long-term constant-stress creep curves for Fe-20Cr-30Ni-2Nb-5Al (at. %) conducted at 760°C under a 35 MPa load in air for durations lasting longer than 500 h. Specimens were homogenized at 1250°C for 24 h and subsequently aged at 800°C for 2.4, 24 or 240 h prior to creep testing.....	60
Figure 4.9: Constant-stress creep curves for Fe-20Cr-30Ni-2Nb-5Al (at. %) as-homogenized at 1250°C for 24 h tested at either 760°C or 700°C under a 35 MPa load..	61
Figure 4.10: BSE images of Fe-20Cr-30Ni-2Nb-5Al (at. %) (a) homogenized at 1250°C for 24 h, then subsequently aged at 800°C for (b) 2.4 h,, (c) 24 h and (d), 240 h and crept at 760°C for 500 h under a load of 35 MPa in air. The light precipitates are the Laves phase and the dark precipitates are NiAl precipitates.....	63

Figure 4.11: BSE SEM images of Fe-20Cr-30Ni-2Nb-5Al (at. %) homogenized at 1250°C for 24 h (a/b) and subsequently aged at 800°C for 2.4 h (c/d), 24 h (e/f) and 240 h (g/h) prior to creep/after creep testing respectively. Constant-stress creep tests were conducted at 760°C for 500 h under a load of 35 MPa in air. The light precipitates are the Laves phase and the dark precipitates are NiAl precipitates.....66

Figure 4.12: BSE images of Fe-20Cr-30Ni-2Nb-5Al (at. %) homogenized at 1250°C for 24 h and subsequently aged at 800°C for 2.4 h and crept at 760°C for 500 h under a load of 35 MPa in air. Both images were taken from the gauge of the specimen with the left taken as a cross-section and the right lengthwise as indicated.....70

Figure 4.13: BSE SEM images of Fe-20Cr-30Ni-2Nb-5Al (at. %) homogenized at 1250°C for 24 h and crept at 760°C for 500 h under a load of 35 MPa in air. The left image was taken from the gauge of the specimen with the left taken from the head as indicated.....72

# CHAPTER 1 INTRODUCTION

## 1.1 Background

Increasing efficiency while decreasing the cost of operating advanced power plants has been an ongoing process. Energy efficiency gains in fossil energy conversion and combustion system applications have the added benefit of reducing CO<sub>2</sub> emissions, bolstering the motivation to pursue efficiency-increasing strategies <sup>1-4</sup>. The efficiency of energy conversion applications is a strong function of steam temperature and pressure, thus increases in energy efficiency can be realized by elevating operating steam temperatures and pressures <sup>5</sup>. An increase in operating temperatures from 600°C to 800°C results in an efficiency increase of more than 10%. Most current coal power plants in the U.S. operate at a maximum steam temperature of 538°C <sup>6</sup>. Advanced ultrasupercritical steam boilers and turbines for power plants offer the promise of higher efficiencies and lower emissions, which are goals of the U.S. Department of Energy's Advanced Power Systems Initiatives. Efforts are currently underway to enable advanced power plants to function at temperatures greater than 700°C <sup>7</sup>. Specifically, the U.S. Department of Energy has set a goal to develop materials technology needed for the construction of the critical components of coal-fired boilers and turbines that are capable of operating with steam at temperatures of 760°C and pressures of 35 MPa, which can reduce emissions, including CO<sub>2</sub>, by 20% or greater compared to today's U.S. power plant fleet <sup>7-9</sup>.

An important contributor to realizing these higher steam temperatures and pressures is the material composition of the power plants' industrial gas turbine

components, super heater tubes and boilers <sup>10</sup>. Currently, many energy production and chemical processing plants operate at temperatures below 600°C due to the poor performance of martensitic and ferritic steel alloys at higher temperatures <sup>11</sup>. To withstand the high temperature and pressure demands of energy applications, metal alloys must have the necessary material properties. These properties include the materials' high-temperature long term creep strength, oxidation resistance and corrosion resistance. Aggressive environments, where metal components are exposed to water vapor, sulfur and carbon species, are a prime target for new materials being developed <sup>12</sup>.

Nickel-based superalloys and austenitic alloys with high nickel concentrations perform well and have the necessary creep strength and oxidation and corrosion resistance to withstand such conditions, but are prohibitively expensive due to nickel's relatively high cost and not economically viable except for use in specialized applications <sup>3,4</sup>. Thus, new iron-based alloys are now being researched and developed that can withstand the demands of energy conversion and combustion systems and decrease reliance on costly nickel-based alloys. However, in order for an alternative to be viable, it must have the strength, long-term creep resistance and oxidation resistance close to or exceeding that of nickel-based alloys. One promising class of alloys that are low in cost and potentially capable of withstanding the rigors placed on the materials by high temperature energy applications are alumina-forming austenitic stainless steels (AFAs) <sup>10, 13-19</sup>. However, more investigation is needed into the oxidation and corrosion resistance as

well as the creep strength in order for this class of steels to be widely used as an alternative to nickel-based alloys.

## 1.2 Alumina-Forming Austenitic Stainless Steels

Extensive efforts are underway to improve the high-temperature strength, corrosion and oxidation resistance, and long-term creep resistance of AFAs, ideally at lower cost compared with currently-used materials. Researchers at Oak Ridge National Laboratory have developed a new family of AFAs in the last few years that have yielded promising results for use at temperatures above 700°C in aggressive environments<sup>12,14,18,20,21</sup>. These new AFAs being developed have a composition range of Fe-(12-35)Ni-(12-15)Cr-(2.5-4)Al-(0.6-3)Nb (wt %), and include alloying additions such as Al, Cr, Mn and Ni to maintain a single phase austenitic matrix microstructure<sup>18</sup>.

The alumina ( $\text{Al}_2\text{O}_3$ ) layer that forms in AFAs at temperatures between 600-900°C, acts as a protective barrier and increases the oxidation and corrosion resistance of the material. Austenitic steels without sufficient additions of aluminum use chromia ( $\text{Cr}_2\text{O}_3$ ) scales as a protective layer, but in environments with high concentrations of water vapor and other oxidizing agents, the chromia scales perform poorly. Relatively small amounts of aluminum additions to austenitic steels have the ability to form the protective alumina surface layer. It's been shown that these alumina scale formations remain stable at operating temperatures from 650-800°C, and have the necessary oxidation resistance in environments with water vapor present, making AFAs the preferred choice for use in low-cost, high-temperature structural materials<sup>10,13,22-26</sup>.

Ferritic FeCrAl alloys have excellent oxidation and corrosion resistance at elevated temperatures, however at temperatures greater than 600°C their creep resistance does not meet expectations set by nickel-based alloys, a property that is attributed to their open body-centered-cubic (b.c.c) structure <sup>18</sup>.

Precipitates play a large role in determining the mechanical properties of an alloy. Both the type of precipitate and its distribution have an effect on an alloy's strength and creep resistance. Precipitate nucleation occurs due to the strain energy being lowered <sup>27</sup>. Precipitates nucleate preferentially on grain boundaries due to a larger strain energy reduction compared with precipitation occurring on dislocations, which has a higher activation energy <sup>28</sup>. The type, size, distribution and volume fraction all have an effect on the alloy's properties. The effect of various precipitates and their phases on creep strength in AFAs is still being explored, to identify the optimum combination of alloys and precipitates for their use at elevated temperatures in the 600°C to 800°C range. Small changes in alloy composition and precipitate phases often result in a wide variation in creep strengths <sup>5,19,29</sup>.

### **1.3 AFA precipitates**

In the past, AFAs have primarily used metal carbides (MC), with the metal primarily being niobium, or  $\gamma'$ -Ni<sub>3</sub>Al for their strength <sup>12,14</sup>. Particles that are ~10 nm in size are effective at increasing creep strength by pinning dislocations in the f.c.c. austenitic matrix. However at temperatures above 800°C, the carbides coarsen and dissolve <sup>30</sup>, making them unsuitable for strengthening purposes in elevated temperature

applications. Newer grades of AFAs being developed have an austenitic face-centered-cubic matrix instead of a b.c.c matrix, and their elevated temperature creep resistance and strength is achieved through not only the existing MC carbides and  $\gamma'$ -Ni<sub>3</sub>Al (L1<sub>2</sub>) precipitates, but also Fe<sub>2</sub>Nb Laves phase and NiAl-type B2 precipitates <sup>10,18,31-33</sup>.

In various Ni-based and Fe-based superalloys, the L1<sub>2</sub>-ordered  $\gamma'$ -Ni<sub>3</sub>Al precipitates are used for their strengthening effects at high-temperatures <sup>19,34</sup>. The f.c.c. structure of Ni<sub>3</sub>Al can be seen in Figure 1.1. In a 2008 study, superior creep resistance in the AFA alloy Fe-20Cr-30Ni-2Nb-5Al (at%) compared to the Fe-15Cr-20Ni-(1-2)Nb (at %) base alloy, was attributed to the formation of a dense dispersion of 30 nm diameter spherical Ni<sub>3</sub>Al precipitates in creep-rupture samples tested at 750°C under a 100 MPa load <sup>20</sup>. Although present at 750°C, Ni<sub>3</sub>Al precipitates were not found in Fe-20Cr-30Ni-2Nb-5Al (at%) at 800°C, negating the precipitates' strengthening effects at temperatures of 800°C or greater <sup>35</sup>. The presence of Ni<sub>3</sub>Al precipitates in the temperature range between 750°C-800°C in the AFA Fe-20Cr-30Ni-2Nb-5Al (at%) alloy has not been evaluated.

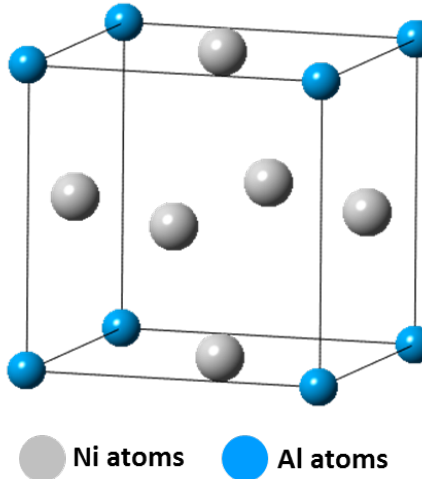


Figure 1.1: Diagram of the  $L1_2$ -ordered  $\gamma'$ - $Ni_3Al$  precipitate crystal structure.

Intermetallic precipitates have the potential to be used as strengtheners in AFA alloys to further improve their creep resistance. The formation of  $Fe_2Nb$  Laves phase precipitates along grain boundaries in ferritic steels resulted in a decrease in the alloys' toughness and yield strength<sup>36</sup>. However, creep strengthening has been achieved in AFAs<sup>12,37</sup>. For example, the AFA alloy Fe-20Cr-30Ni-2Nb-5Al (at%) demonstrates good ductility and strength, even with extensive  $Fe_2Nb$  Laves phase precipitates along the grain boundaries<sup>38</sup>. It has been shown that in Fe-20Cr-(25–35)Ni-2Nb (at.%) alloys, fine dispersions of strengthening  $Fe_2Nb$  Laves phase can form within the austenitic iron matrix<sup>39</sup>. The  $Fe_2Nb$  particles in this alloy are thermally stable up to its melting point of 1640°C over a prolonged duration<sup>40</sup> and exist in equilibrium with f.c.c.  $\gamma$ -Fe above 955°C in the Fe-Cr-Ni base steel<sup>41</sup>, making them a good candidate for strengthening AFAs at elevated temperatures.

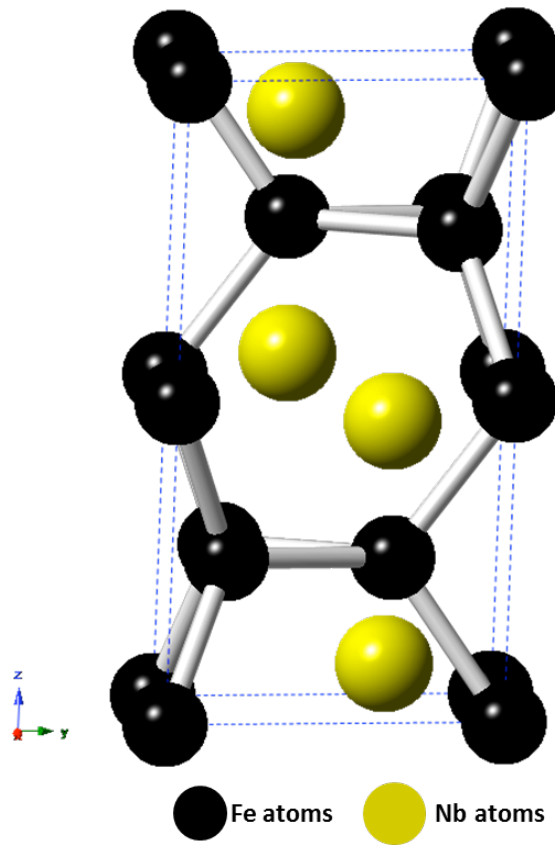


Figure 1.2: Diagram of the hexagonal C14  $\text{Fe}_2\text{Nb}$  Laves phase structure.

Prior work with the intermetallic Laves phase  $\text{Fe}_2\text{Nb}$  has shown that the strengthening effect of the precipitate is dependent on whether it precipitates on grain boundaries or in the austenitic matrix, and in what volume fractions and particle size it appears in the alloy<sup>20</sup>. See Figure 1.2 for a diagram depicting the hexagonal C14  $\text{Fe}_2\text{Nb}$  Laves phase structure. As the Laves phase particles increase in density and size, the brittle properties of the precipitate cause the material to lose its strength and creep resistance. Thus, a fine particle dispersion diameter of <100 nm is recommended to match

the creep strength exhibited by AFAs strengthened with MC carbides and prevent failure of the material <sup>20</sup>. The decrease in the precipitate size and increase of the precipitate volume fraction in the austenitic matrix, permits dislocations to be pinned, leading to an increase in the alloy's creep strength. It has recently been shown by Tarigan et al. that in Fe-20Cr-30Ni-2Nb (at.%), the alloy's long-term creep resistance increased with an increasing area fraction of Laves phase precipitated on the grain boundary. It was also noted that dislocations that piled up near Laves phase grain boundaries were effective at suppressing local deformation by inhibiting the motion of dislocations and thereby increasing the long-term creep strength of the alloy <sup>42, 43</sup>. This creep-strengthening mechanism was coined "*grain boundary precipitation strengthening mechanism*" by Tarigan et al.

Yamamoto et al. found that in addition to  $\text{Fe}_2\text{Nb}$  Laves phase forming after heat treating at 750°C, dense and fine B2-type NiAl precipitates formed in the  $\gamma$ -Fe matrix and on the grain boundaries <sup>21</sup>. The B2-type NiAl phase particles, which were dark in contrast in backscattered electron images, were between 300 nm and 1  $\mu\text{m}$  in size. The  $\text{Fe}_2\text{Nb}$  Laves phase particles appeared spherical with a bright contrast in the matrix, and were less than 500 nm in size. See Figure 1.3 for an example of precipitate contrast in Fe-20Cr-30Ni-2Nb-5Al (at. %). At elevated temperatures, B2-type NiAl precipitates play an important role in providing corrosion and oxidation resistance by acting as an aluminum reservoir for the formation of the alumina protective layer <sup>44</sup>. They are not effective in improving the high-temperature tensile strength at temperatures greater than 400°C <sup>45,46</sup>,

however it's been posited that B2-type NiAl precipitates improve creep resistance by either affecting the climb of dislocations in the matrix or by limiting crack propagation during creep deformation due to the precipitates' discontinuous and granular-shape<sup>21</sup>.

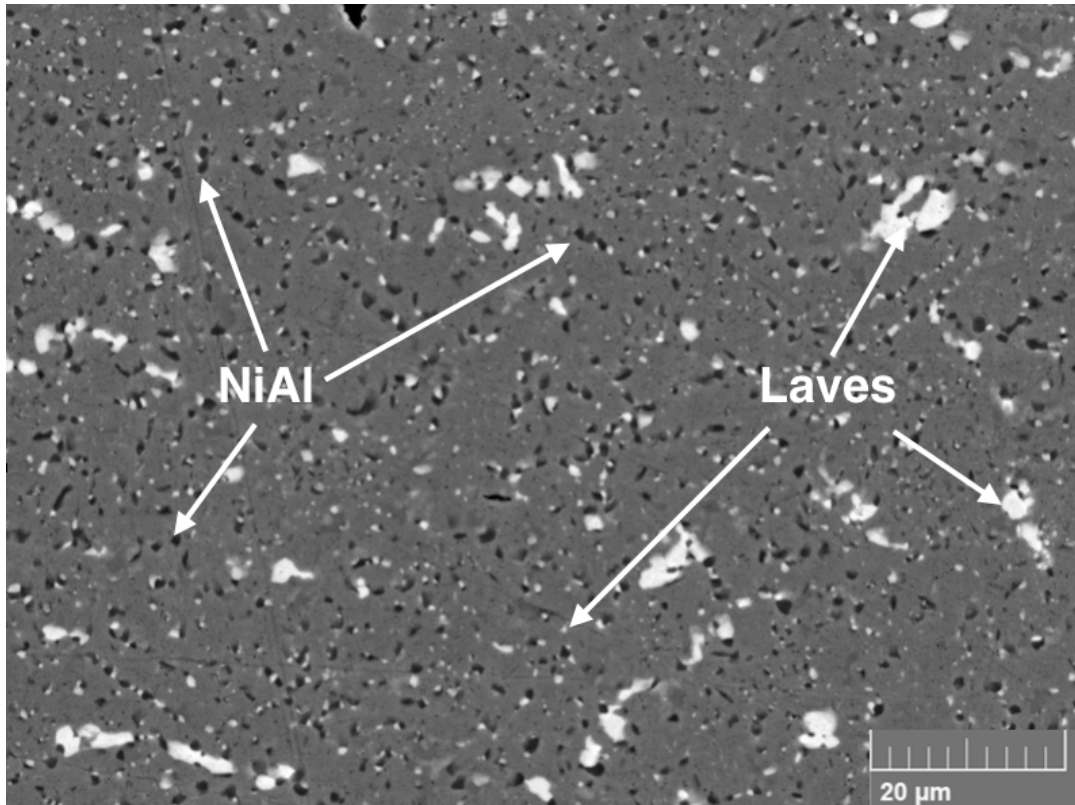


*Figure 1.3: Backscattered electron image showing  $Fe_2Nb$  Laves phase (light contrast) and B2-type NiAl phase (dark contrast) precipitates in the matrix of Fe-20Cr-30Ni-2Nb-5Al (at. %) homogenized at 1250°C and heat-treated at 800°C for 240 h.*

Trotter et al. studied the effect of aging on the microstructure and mechanical behavior of Fe-20Cr-30Ni-2Nb-5Al (at%).<sup>38</sup> They found that the alloy was fully homogenized and presented as single phase austenite (f.c.c.) after a solutionizing anneal

at 1250°C for 24 h, and that there was increasing amounts of B2 and Laves phase precipitation with successively longer heat treatments at 800°C conducted for a variety of time intervals lasting 0, 2.4, 24, 240 and 1325 h. The 1250°C homogenization temperature was chosen by Trotter et al. after considering the Fe-Cr-Ni-Nb quaternary system at 1200°C as well as from illustrations of the phase equilibria. The homogenization and heat treatment conditions for this study were therefore chosen to enable comparison with the results of and to mimic the successful temperatures and durations chosen by Trotter et al.<sup>38,52</sup> Heat treatments lasting a duration of 1325 h were not conducted in this investigation, because previous studies' findings indicated that results did not differ greatly from the 240 h anneal.

In order to better predict which precipitates are most beneficial for increasing AFA high temperature creep strength, further tests and characterization needs to be performed to obtain a better understanding of the complex interactions between the presence of various precipitates and phases and their effect on the alloys' creep properties.

#### **1.4 Outline of Research Project**

The purpose of this thesis is to investigate the high-temperature strengthening mechanisms in alumina-forming austenitic stainless steels, specifically the high temperature constant-stress creep and mechanical properties of the model alloy Fe-20Cr-30Ni-2Nb-5Al (at. %) at different aging conditions.

The investigation proceeded as follows:

- 1) A constant-stress creep rig was designed, built and its operation validated
- 2) Samples were prepared from the model alloy and aged for time intervals of 0, 2.4, 24 or 240 h at 800°C
- 3) Constant-stress creep tests were conducted at elevated temperatures of 760°C at a stress of 35 MPa.
- 4) Secondary electron imaging was used to examine the microstructure of the samples prior to and after the completion of creep testing
- 5) Elevated temperature tensile tests were conducted on aged samples at 760°C

Chapter 2 focuses on the design, construction and testing of the constant-stress creep rig used in this investigation.

Chapter 3 covers materials preparation, testing procedures and materials characterization techniques.

Chapter 4 describes the effect of aging time on the microstructural evolution and high temperature constant-stress creep and tensile behavior of the model alloy. The observed microstructural changes and precipitate evolution prior to and after creep tests were conducted, are analyzed and discussed. Additionally, the observed differences in the mechanical properties of the alloy after different aging conditions were explored.

In Chapter 5 and 6, the conclusions of this research project are summarized and suggestions are made for future work.

## CHAPTER 2      CONSTANT-STRESS CREEP RIG DESIGN AND CALIBRATION

### 2.1      Introduction

This chapter details the design and calibration of a constant-stress creep rig constructed for use in this investigation to conduct high temperature constant-stress creep tests.

### 2.2      Overview of Constant-Stress Creep Machines

Creep testing machines take several forms depending on what is the primary target of investigation, which includes constant load, variable stress and constant-stress rigs. A small change in the level of stress can have a large effect on strain rate affecting both the overall creep rate and microstructure of the sample. With increasing strain, the cross-sectional area  $A$  of a test specimen decreases, which if tested in a constant-load creep rig, results in an increase in the instantaneous stress. With a load  $P$ , cross-sectional area  $A$ , the stress on the specimen will be  $\sigma = P/A$ . A constant-stress machine would allow the stress variable to be controlled by compensating for the decrease in the specimen's cross-sectional area by decreasing the effective load applied on the specimen. This allows the basic creep mechanisms acting on the specimens tested to be isolated and analyzed.

The curvature of the constant-stress cam is key to constructing a precise, operational constant-stress creep rig. In Figure 2.1, a schematic layout of the weight-transferring system is shown for a constant-stress creep test applications. For constant-load creep tests, the curved cam would be circular.

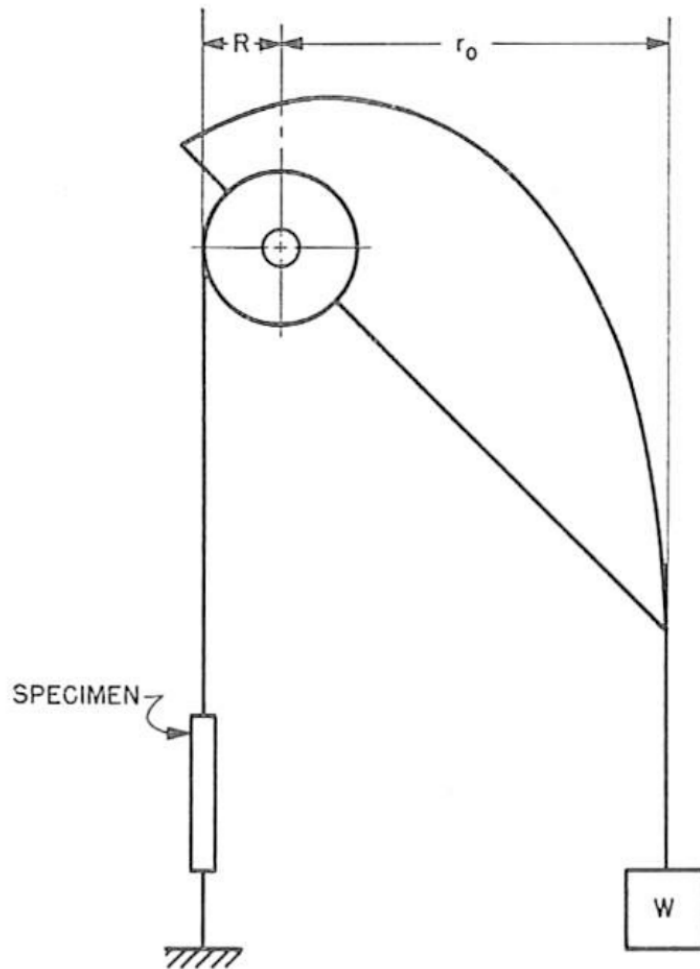


Figure 2.1: A schematic diagram detailing a weight-transferring system used for constant-stress creep tests.<sup>47</sup>

The curved profile of the constant-stress cam is analytically calculated using a system of parametric equations following the outline of an Andrade-Chalmers beam<sup>48</sup>. It is shown that the fixed Cartesian coordinates  $x$  and  $y$  of a constant-stress cam can be written in terms of constants and the angle  $\theta$  (see Appendix I for derivation of equations (1) and (2)), where  $\theta$  is the angle the cam makes with the horizontal as seen in Figure 2.2

from the paper by Garofalo et al (1962). In equations (1) and (2)  $L_0$  is the initial specimen gauge length prior to creep,  $r_0$  is the initial moment arm,  $R$  is the radius of the smaller load-transferring wheel. The Cartesian coordinates from which the profile of the cam can be traced for machining are determined by the values of constants  $a$  and  $b$ :

$$a = \frac{r_0 L_0}{L_0 - R\theta_0} \quad \text{and} \quad b = \frac{R}{L_0 - R\theta_0}$$

$$x = \frac{a}{1 + b\theta} \left[ \cos(\theta) + \frac{b \sin(\theta)}{1 + b\theta} \right] \quad (1)$$

$$y = \frac{a}{1 + b\theta} \left[ \sin(\theta) - \frac{b \cos(\theta)}{1 + b\theta} \right] \quad (2)$$

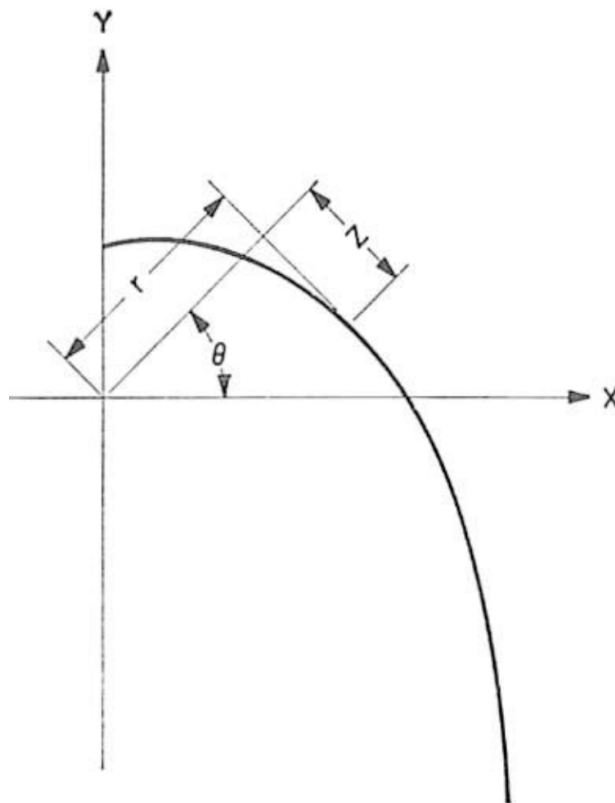


Figure 2.2: A diagram detailing the coordinate system used for the cam profile

For the purposes of this investigation, a constant-stress creep test rig was custom-designed, built and its operation validated based on the methods developed by Garofalo, Richmond and Domis (1962). The following section discusses the system's dimensions, assembly, cam parameters, calibration and testing procedure.

### **2.3 Design of Creep Test Rig**

A photograph of the full assembly of the creep rig is shown in Figure 2.3 with a sample specimen in tension and placed under a 35 MPa load.

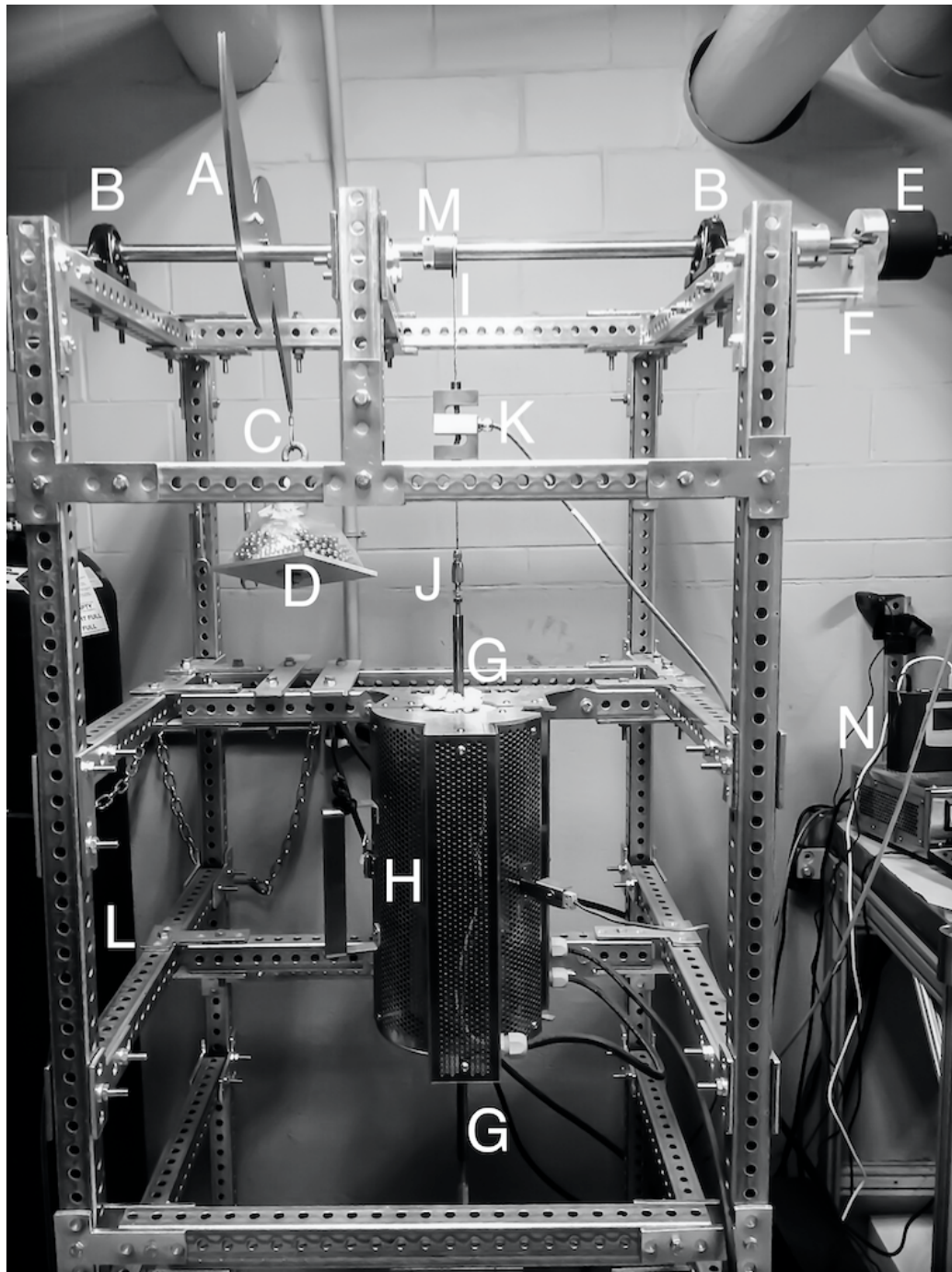


Figure 2.3: Photograph of the constant-stress creep machine with system components labeled matching the key

Key for Figure 2.3

- A. Constant-stress cam
- B. Bearing pillow block
- C. Cable attached to load
- D. Load weight on loading tray
- E. Angular Displacement Transducer (ADT)
- F. ADT support
- G. Connecting rod
- H. Mellen Furnace
- I. Cable attached to specimen
- J. Swageless Thread Terminal
- K. Linear variable differential transformer (LVDT)
- L. Steel Frame
- M. Load-transferring wheel
- N. Data Logger

*\* Letters in parentheses () indicate machine components as per Figure 2.3*

### 2.3.1 *Frame and Mounts*

The metal frame (L) of the rig is made of 1.5-in galvanized steel perforated tubing for heavy duty telescoping framing and is bolted onto four base mounts to account for uneven floor surfaces. The metal frame additionally supports the Mellen Inc. SCR Split Series 120 V 1200 W Furnace (H) mounted vertically. The furnace utilizes clamshell-heating elements capable of 1250°C in air. The temperature is measured with a centrally located K-type thermocouple and controlled by a Mellen Inc. PS105 programmable power control cabinet. Two heavy-duty ball bearing pillow blocks (B) are rigidly attached to the steel frame and support a 0.75-in diameter steel rod that acts as the cam and load-transferring wheel support shaft.

### 2.3.2 *Constant-Stress Cam*

As discussed in the previous section, the cam profile is dictated by the constants  $a$  and  $b$ . For a small load-transferring wheel with a radius of 0.75 inches, an initial specimen gauge length of 0.787 inches and a desired mechanical advantage of 8:1, the values of  $a = 6.00$  in and  $b = 0.95$  in. Using the derived equations (1) and (2) and the calculated values of  $a$  and  $b$ , the Cartesian coordinates of the cam's profile in  $x$  and  $y$  can be calculated for a given angle  $\theta$  as shown in Table 2.1.

Table 2.1 Coordinates for the constant-stress cam profile fabricated for use in this study, with  $a = 6.00$  in and  $b = 0.95$  in.

$\Theta$ (deg)	x (in)	y (in)
-20	4.06	-15.13
-15	5.10	-11.87
-10	5.66	-9.35
-5	5.93	-7.34
0	6.00	-5.72
5	5.94	-4.37
10	5.80	-3.24
15	5.59	-2.29
20	5.33	-1.48
25	5.05	-0.79
30	4.74	-0.20
35	4.42	0.30
40	4.09	0.74
45	3.75	1.10
50	3.41	1.41
55	3.08	1.67
60	2.74	1.89
65	2.42	2.06
70	2.10	2.19
75	1.78	2.29
80	1.48	2.35
85	1.19	2.39
90	0.92	2.40
95	0.65	2.39
100	0.40	2.36
105	0.17	2.31
110	-0.05	2.24
115	-0.26	2.15
120	-0.45	2.05
125	-0.62	1.94
130	-0.78	1.82
135	-0.92	1.69
140	-1.05	1.55
145	-1.16	1.41
150	-1.25	1.26
155	-1.33	1.11

The constant-stress cam (A) and the load-transferring wheel (M) are mounted on the steel rod with a diametrical interference fit of 0.003-in, which facilitates free circular movement around the rod. The cam profile shown in Figure 2.1 is duplicated, inverted and attached to the original cam profile to balance the cam assembly when it's threaded onto the support rod. The small radius load-transferring wheel is designed for an 8:1 mechanical advantage. Both the cam and the wheel are attached to the center support shaft with a collet and two set screws placed on opposing sides and screwed in to firmly secure the components and eliminate movement when the system is under load. The cam and the load-transferring wheel are fabricated from 1018 steel. Appendix II contains CAD drawings with specifications of the cam and load-transferring wheel.

### 2.3.3 *Angular Displacement Transducer*

The TransTek Inc. Series 600 Model 0603-0000 Angular Displacement Transducer (ADT) with 100 mV/degree output and maximum usable range of  $\pm 40^\circ$  is attached (E) with a set screw to the end of the support shaft extending 1 inch past the pillow block and steel frame tubing. The ADT allows for measuring the specimen elongation by tracking the angular displacement of the cam shaft as the sample lengthens throughout the duration of a creep test. More specifically, as the specimen creeps, the relative displacement of the two specimen grips is detected by the ADT. This angular displacement is translated into an electrical signal, which is then amplified by the TransTek Inc. Series D100 Dual DC 12VDC Power Supply and sent by the readout wire to the Grant Instruments Ltd. SQ2010 Portable Universal Input Squirrel

Data Logger (N) to monitor, measure and record the elongation of the specimen. The high accuracy ADT is capable of measuring an angular displacement of  $\pm 0.10\%$ , which translates to measuring a linear displacement of  $<0.001$  in. The ADT is supported with an aluminum bolted frame (F) to eliminate any torque placed on the high-precision measurement equipment.

#### *2.3.4 Cable and Load Alignment*

Both the constant-stress cam and the load-transferring wheel have a 0.047-in radius milled groove tracing their outer profile to create a track that allows for a 3/32-in wire cable to fit and wrap around with a snug fit. A wire 3/32-in cable (C) is attached to the constant-stress cam through a pinhole, shown in Figure 2.4, and swaged together with wire rope sleeves. The other end of the cable is swaged in a loop and permits the attachment of a dead-weight load. The load is attached through the use of an 8-inch long metal hook threaded through the center of an aluminum 6x6-in square platform (D). The load is stacked on the platform. Steel 1/4-in diameter balls are used for ballast to aid in applying a variety of loads with precision.

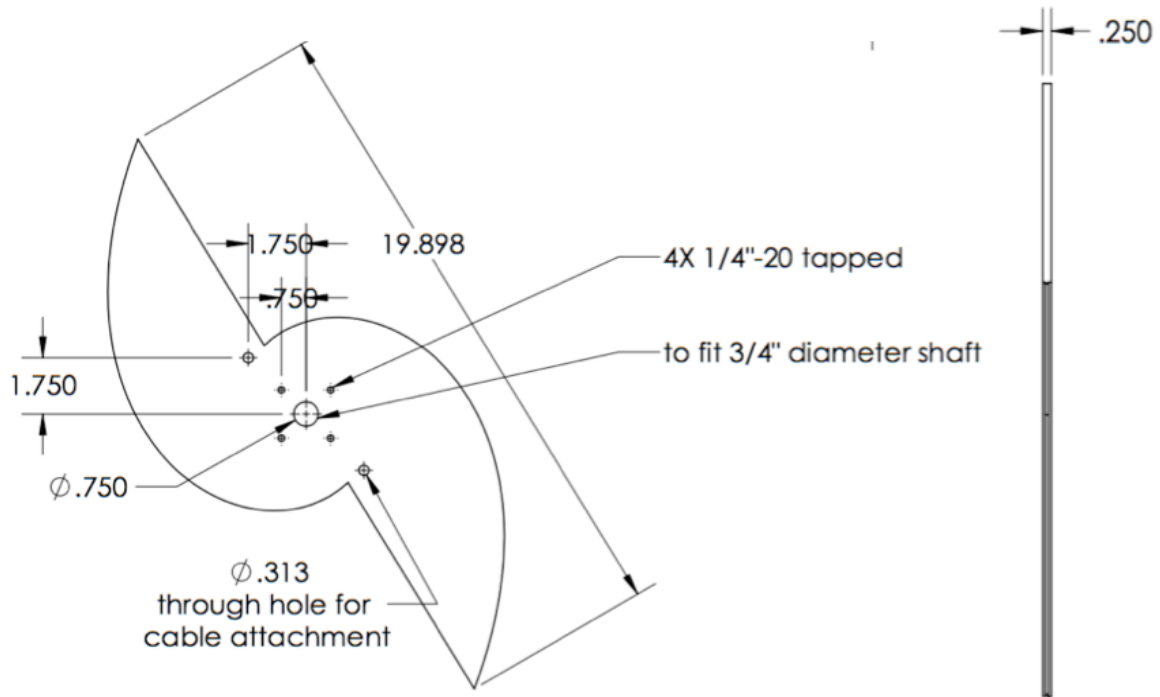
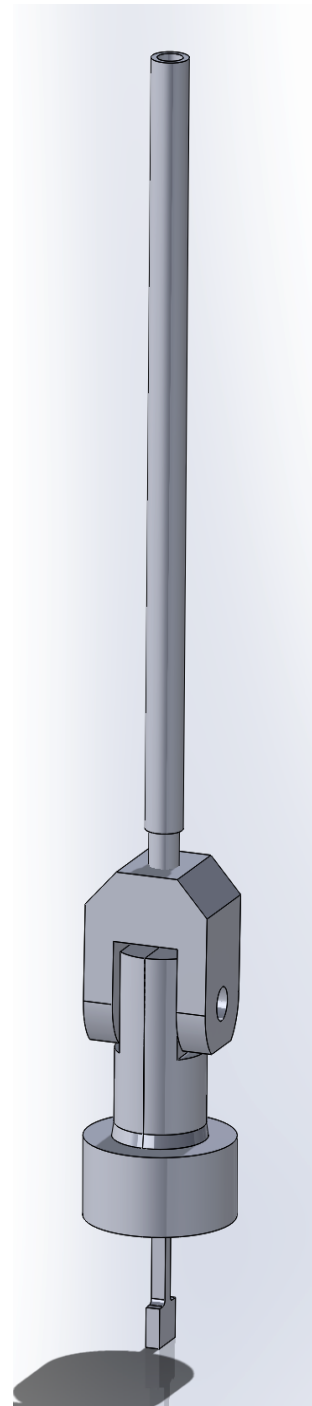


Figure 2.4: Design drawing of constant-stress cam

One end of a wire 3/32-in cable (I) is attached and swaged through a pinhole to the load-transferring wheel (M) on the opposite side that the cable is attached to the constant-stress cam. The other end of the cable drops vertically down to connect through two attachment openings in the vertically aligned Omega Engineering Inc. LC101-500: 500 lb S-beam load cell (K), which acts as the linear variable differential transformer (LVDT). The LVDT output wires are connected to the data logger (N) and Omega Engineering Inc. DP25B-S-A series Digital Panel Meter with a 4-digit LED display that aids in adjusting the cam placement when a load is applied by displaying the output in lbf units. A wire cable is attached through the bottom of the LVDT to a swageless thread terminal (J).

### 2.3.5 *Specimen Grip Components*

The thread terminal is screwed into the machined upper extension connecting rod (G). The extension rod is screwed into the upper male end of the machined specimen grips as shown in Figure 2.5. The specimen grips and connecting rods are fabricated from 718 Inconel to prevent elongation when heated in the furnace, and hold the specimen in a vertically aligned position. The lower specimen grips are similarly connected to an extension rod, a swageless thread terminal and a wire cable. Figure 2.5 shows a diagram of the details of the specimen grips. Appendix II contains CAD design drawings of the grip components, which includes the inner grips, collets, yolks, and rod connectors.



*Figure 2.5: Diagram of specimen grips*

### 2.3.6 *Making Adjustments*

Completing the linkage, the wire cable is vertically secured to the bottom crossbeam of the steel frame in a 1/4-in diameter slot to allow for lateral movement and adjustments of up to 2 inches when a load is applied to the system and the cable is placed under tension.

Of special note is the horizontal position mark that is inscribed on the constant-stress cam prior to the system assembly. The cam is designed to produce a constant-stress about this centerline as shown in Figure 2.6, which aids in proper adjusting and positioning of the cam during calibration testing such that the rig functions as intended (refer to Calibration Testing section 2.4.4).

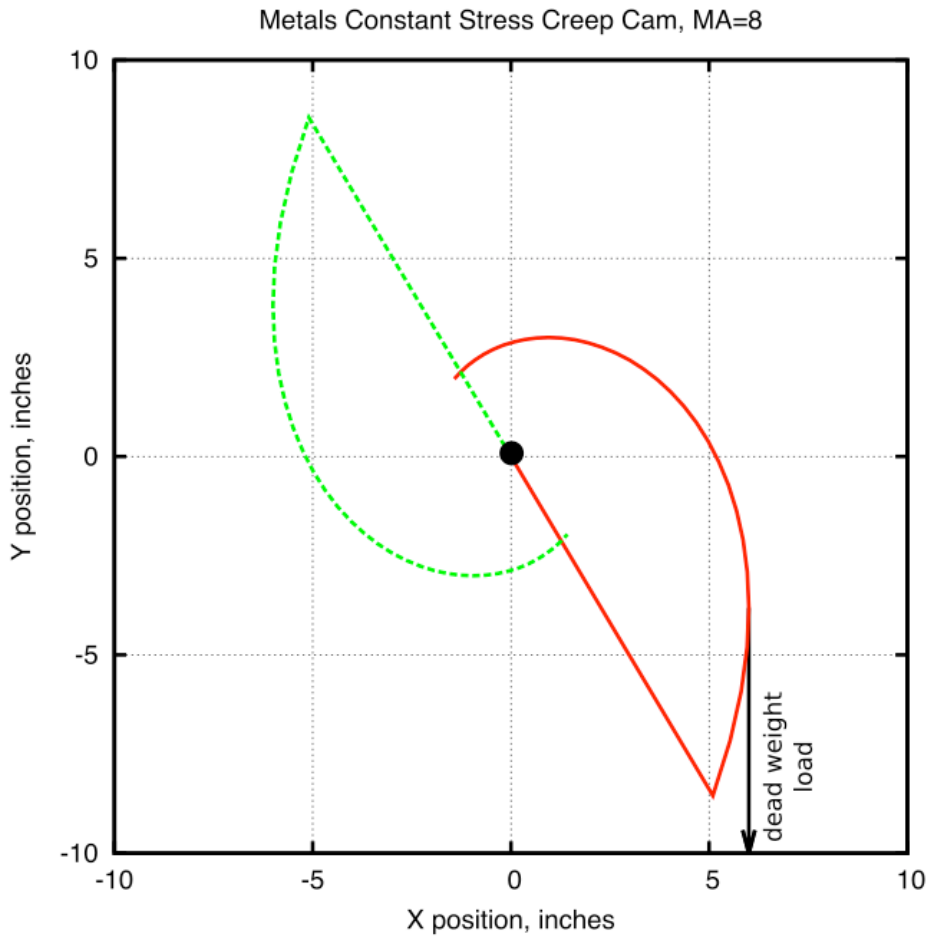


*Figure 2.6: Plot of the constant-stress cam geometry. The cam's centerline is centered on  $y = 0$ .*

### 2.3.7 Data Logging

The Squirrel data logger receives amplified voltage readouts from the ADT and LVDT. The output is sampled at five-second intervals and then logged as an average of five samples. This logging rate allows for long term creep tests to be conducted by decreasing the amount of data logger memory used, while ensuring the data collected has appropriate resolution for detailed data analysis.

## 2.4 Testing and Verification

A range of tests were performed on the creep rig to verify that the system functioned as intended. The machine was calibrated for use with a load of 35 MPa, and a series of tests were conducted to prove that the load on the test sample would be reduced at the specified rate to produce a constant-stress.

### 2.4.1 Identifying the ADT Adjustment Factor

The Angular Displacement Transducer (ADT) output is a voltage, which is converted to an angular displacement in degrees. This rotational displacement value is used to calculate the elongation of the test specimen to a high degree of precision. The ADT displacement measurements required an adjustment factor to match the actual test specimen elongation.

To conduct the test and acquire the adjustment factor, a sample test specimen was placed in the system and the effective load was decreased in 5 MPa increments by mechanically simulating a displacement of the specimen, which was accomplished by unscrewing the upper connecting rod out of the upper specimen grip connector. The data logger was used to record the angular displacement recorded by the ADT, and a micrometer was used to measure and record the simulated linear displacement. The test was conducted three times and the data was averaged. Figure 2.7 shows the results of this calibration.

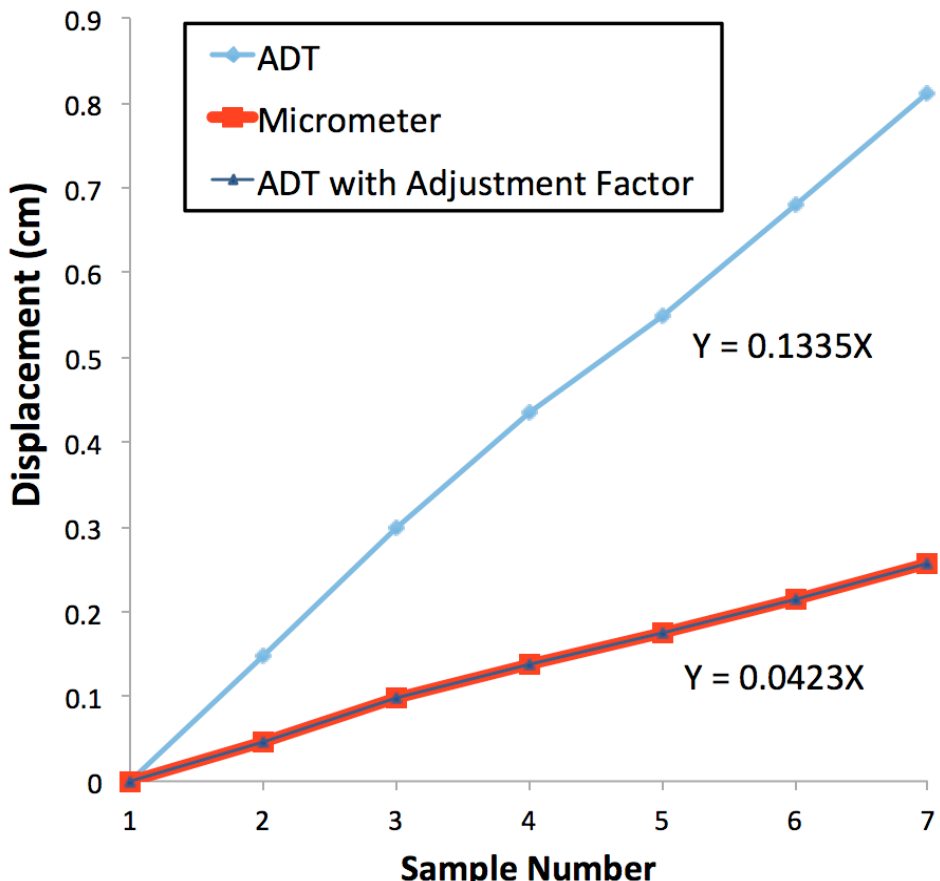


Figure 2.7: Plot of system displacement measurements taken with ADT, manually with a micrometer and the same ADT results plotted with an adjustment factor. Notice the adjusted ADT measurements match those taken with the micrometer.

When the ADT results were adjusted with a factor of 3.156, the displacement values were identical to those taken with the micrometer. This verified that the system recording displacement accurately measured and recorded specimen elongation.

#### *2.4.2 Eliminating Creep Contributions From System Components*

A test was performed to determine if the connecting components of the system, such as the connecting rods, cable and grips, would creep under an applied load and affect the test results by contributing to the overall creep measured.

A sample T-bone was fabricated from 718 Inconel and heat treated, which is the same material from which the specimen grips and connecting rods were fabricated. The sample was inserted into the specimen grips and the system put under a load of 35 MPa (the load used for subsequent testing in this investigation). The system was tested for 24 h. An initial displacement was recorded by the ADT within the first few seconds of the system coming under load, which can be attributed to the elimination of slack in the system.

No creep of the system components was detected for the duration of the 24 h period. This demonstrated that the only contributing factor to subsequent tests' resulting creep was attributed to elongation of the T-bone specimens and not to the creep of components of the system.

#### *2.4.3 Furnace Temperature Profile*

The furnace to heat the sample at a constant temperature was vertically aligned and therefore its temperature profile was measured to ensure that the temperature experienced by the test specimen was indeed the temperature set point being measured by the K-type thermocouple in the furnace.

A second thermocouple was inserted along the inside length of the furnace and used to identify the location at which the measured temperature matched that being displayed as the set point on the furnace power control cabinet. This test was repeated three times and the results averaged with a final location determined to be 5.5 inches measured from the top of the furnace tube or 6.5 inches measured from the tube bottom exit. The system cables were adjusted accordingly to ensure that when under load, the test specimen would be located at the target height.

#### *2.4.4 Calibration Testing*

For a constant-stress test, the equation:

$$P/P_0 = L_0/L \quad (1)$$

where  $P$  is the load and  $L$  is the length of the specimen, must be satisfied for any angle and for any initial load  $P_0$  in order to satisfy the requirement that  $PL = \text{constant}$ . The creep rig was calibrated by comparing the theoretical predictions of equation (1) with experimental measurements of  $P$  and  $L$ .

Before beginning the calibration test, the cam was adjusted so the horizontal position mark inscribed on its side was level and at the intended zero mark. The furnace door was propped open to expose the specimen grips inside and a test specimen inserted. Steel balls with a total load 35 MPa were placed onto the loading tray. A zero reading was taken and recorded. The angle was increased in 5-degree increments, by mechanically simulating a displacement of the specimen, from 0 to 35 deg. For each interval, the load and linear displacement were recorded.

Figure 2.8 shows the calibration plot. The experimental values had an average variation of 0.36 percent compared to the theoretically predicted values from equation (1). This value was well within the bounds of literature values<sup>47</sup> confirming the rig was calibrated and operational for constant-stress testing.

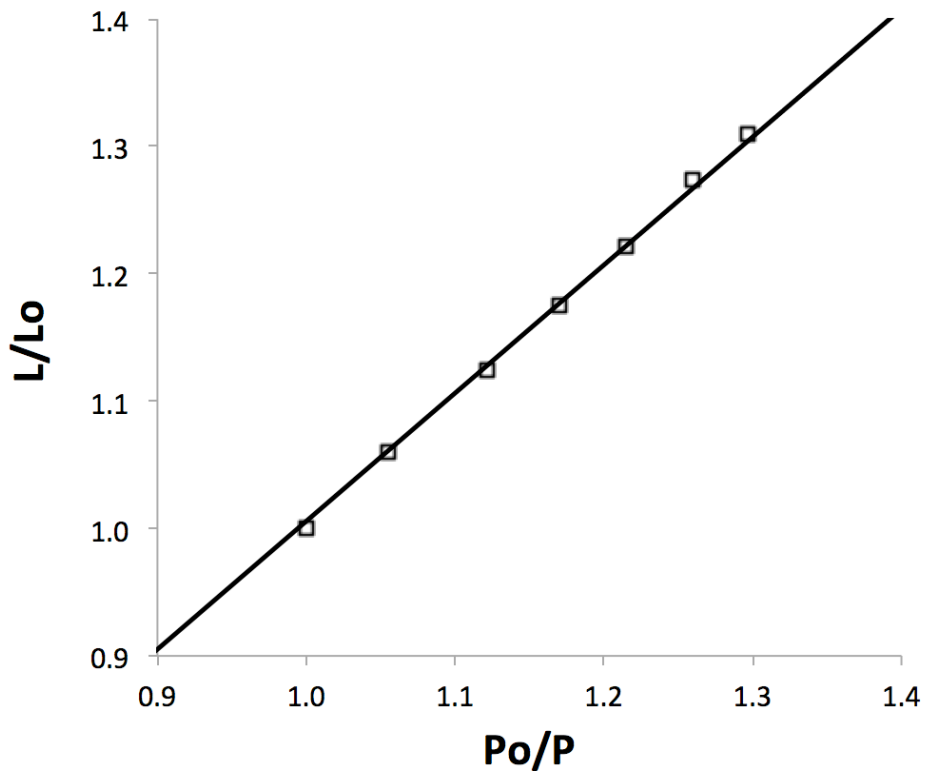


Figure 2.8: Load calibration of constant-stress cam

## CHAPTER 3      EXPERIMENTAL METHODS

### 3.1      Introduction

This chapter details materials preparation and processing methods, constant-stress creep testing procedures, tensile testing and materials characterization techniques involved in this work.

### 3.2      Materials Preparation

#### 3.2.1    *Materials Used*

The alloy Fe-20Cr-30Ni-2Nb-5Al (at.%) was used for both the creep and tensile tests throughout this study. The alloy was provided by Mr. Michael Schmidt, Carpenter Technology Corporation (Wyomissing, PA). A split-cast vacuum induction melting heat was used to cast the alloy into 8 kg tapered ingots. The ingots were then press forged into rectangular bars with the following dimensions: 1.58 cm x 1.91 cm x 60.9 cm. The chemical composition of the alloy was analyzed by LECO combustion analysis and X-ray Fluorescence. Table 2.1 compares the analyzed element compositions with the theoretically calculated weight percent ratios, demonstrating agreement between the predicted and actual chemical composition of the cast alloy.

*Table 3.1 Alloy compositions obtained by chemical quantitative analyses*

<b>Element Analyzed</b>	<b>Theoretical (wt%)</b>	<b>Analyzed (wt%)</b>
Nickel	31.88	31.9
Chromium	18.83	18.98
Niobium	3.36	3.34
Aluminum	2.44	2.48
Carbon	0.00	0.02
Cobalt	0.00	0.01
Copper	0.00	<0.01
Manganese	0.00	<0.01
Molybdenum	0.00	0.01
Phosphorus	0.00	<0.005
Silicon	0.00	<0.01
Sulfur	0.00	<0.001

### 3.2.2 Sample Machining

In preparation for both creep testing and tensile tests, the alloy was machine milled and then sectioned with a saw. The TRAK DPM SX3P bed mill with a 40 taper spindle and ProtoTRAK SMX control was used with zinc-coated carbide end mills to mill the specimens into the T-bone shapes necessary to insert into the specimen grips of the creep testing and tensile testing machines as shown in Figure 3.1. To ensure the accurate geometry of each T-bone, the specimen was sectioned using coolant with a Model 650 Low Speed Diamond Wheel Saw from South Bay Technology, Inc.

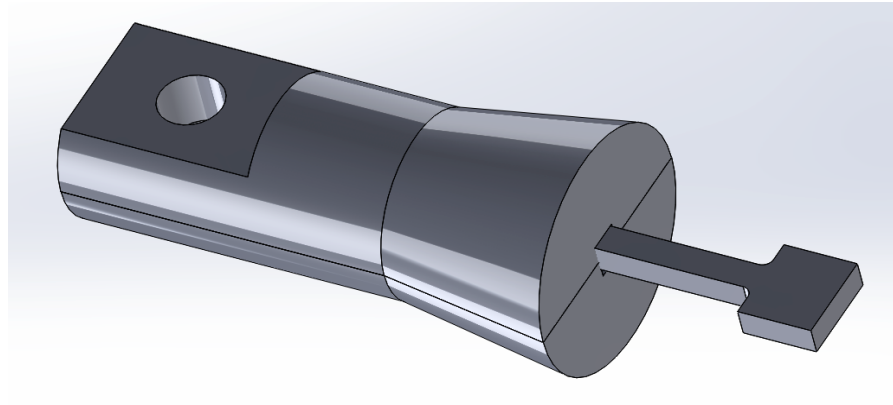


*Figure 3.1: CAD file drawing of a T-bone specimen inserted into one side of the creep machine's specimen grips.*

### 3.2.3 Material Homogenization

Solutionizing anneals were necessary to homogenize the material for a uniform microstructure. For all tests in this study, the as-cast model alloy was homogenized for 24 h at 1250°C under vacuum and then water-quenched. This temperature and time was chosen with consideration to prior work with Fe-20Cr-30Ni-2Nb-5Al, where it was determined that a solutionized single phase  $\gamma$ -matrix could be consistently formed.<sup>38</sup> This was confirmed with SEM images of the as-cast raw material and compared with the material after a heat treatment homogenization conducted at 1250°C for 24 h.

All solutionizing heat treatments were conducted using a Thermo Scientific Type 54233 Lindberg Closed-Shell tube furnace. Specimens were placed on top of a piece of alumina and maneuvered to the center of the furnace tube with a rod. The furnace tube was then purged with argon and placed under a pressure of 0.01 MPa to maintain an oxygen-free environment and to prevent oxidation of the sample inside the furnace until

the heat treatment was complete. Once the sample was sealed inside the furnace, the furnace was turned on and the temperature set to 1250°C. When the solutionizing anneal was complete, the pressure seal was broken and the sample rapidly quenched in water having a substantially greater mass compared to the sample.

#### 3.2.4 *Annealing*

All heat treatments of the samples after they were homogenized were conducted at 800°C for a variety of time intervals of 0, 2.4, 24 or 240 h to capture a breadth of aging conditions. Heat treatments were conducted in a Barnstead Thermolyne Type 47900 Furnace. Samples were placed inside an alumina crucible and then positioned at the center of the furnace for the duration of the heat treatment. At the completion of the heat treatment, the samples were quenched with water.

### 3.3 Materials Characterization

#### 3.3.1 *Scanning Electron Microscopy*

In preparation for imaging with the scanning electron microscope (SEM), samples were compression mounted and polished on a turntable using successively finer silicon carbide abrasive paper up to 1200-grit, then with 0.3  $\mu\text{m}$  followed by a finer 0.05  $\mu\text{m}$  alumina powder dissolved in water. Samples were placed on a polishing vibrometer with a thin layer of diluted MasterMet Colloidal Silica Polishing Suspension solution for ~3 h to eliminate surface defects and achieve a mirror finish. After the polishing was complete, the samples were washed with a spray of distilled water, then methanol,

followed by a light scrubbing with a cotton swab and detergent to eliminate any adhered alumina particles.

Samples were imaged using a Tescan Vega3 SEM outfitted with Bruker Quantax Energy-dispersive X-ray Spectroscopy (EDS) and electron backscatter diffraction (EBSD) detectors. Samples were imaged using back-scattered electrons (BSE) with a working distance of 10 mm and operating voltage of 15 keV. To distinguish the matrix, NiAl and Laves phase precipitates, BSE images were used for microstructural analysis due to the strong BSE contrast based on atomic number.

For quantitative analysis, particle density and average particle diameter were analyzed using ImageJ image processing software (Wayne Rasband, NIH). BSE images were taken at 4000x and pre-processed to optimize uniformity of illumination and contrast in the input images. This step consisted of reducing artifacts generated by the acquisition system, contrast enhancement, despeckling and setting the threshold at a level that allows for differentiation between the lighter, brighter-contrasted Laves phase particles and the darker-contrasted NiAl precipitates. After the proper threshold was established, images were processed with outlier filters. Particle diameter and density were calculated using ImageJ open source plugins. Areas with low pixel counts corresponding to particles with diameters <80 nm were excluded from the analysis.

### 3.3.2 *Transmission Electron Microscopy*

For thin-film TEM examination, material was prepared by sectioning discs from samples that were milled into the form of 3 mm diameter cylindrical rods. The specimens were ground and mechanically polished to a thickness of  $\sim$ 0.2 mm. They were electrolytically thinned in a polishing electrolyte solution consisting of 20% nitric acid and 10 % butoxyethanol in methanol in the temperature range of -20 to -25°C using the Struers TenuPol-5 apparatus with a voltage of 10 V and current of  $\sim$ 50 mA. After being electropolished, the samples were rinsed three times with ethanol.

The resulting samples were placed in a double-tilt holder with a capability of tilting 60° along two axes in order to adjust the specimen orientation during analysis. TEM investigations to characterize the microstructure of the material were performed using a FEI Tecnai F20 FEG-TEM under an accelerating voltage of 200 kV.

## 3.4 Constant-Stress Creep Testing

### 3.4.1 *Sample Preparation*

Following verification and calibration of the creep rig as described in section 2.4 of Chapter 2, creep test specimens were milled from the Fe-20Cr-30Ni-2Nb-5Al (at. %) model alloy to a 3 mm thickness, with a gauge length of 20 mm, width of 3mm and overall length of 35 mm as shown in Figure 3.2. Each specimen was homogenized for 24 h at 1250°C to produce single-phase material. Specimens were subsequently aged in air at 800°C for 0, 2.4, 24 or 240 h.

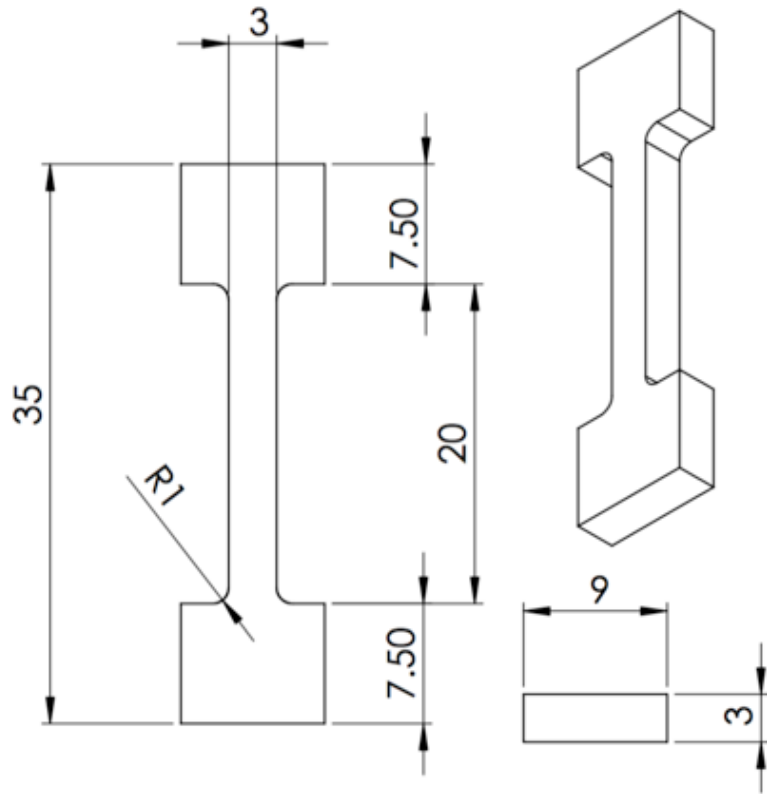


*Figure 3.2: Dimensions of creep test specimen in millimeters.*

Prior to conducting creep tests, one representative sample from each heat treatment procedure was mounted, polished and imaged using the SEM as detailed in section 3.3.1. These imaged samples provided a baseline for each heat treatment to compare to the specimen microstructures after they had undergone a creep test.

#### *3.4.2 Creep Test Experimental Procedure*

Test specimens were inserted into the high temperature specimen grips and the furnace door locked. Glass wool was placed over the top and bottom furnace openings to reduce air currents and increase temperature uniformity throughout the furnace. 4.015 kg

of steel balls were placed on the loading tray for a total load of 35 MPa, but it was not attached to the cam cable wire attachment loop. The cam was set so that the inscribed horizontal position mark was level, and the furnace was set to 760°C. This temperature was chosen for all creep tests, because it matches the target application temperature for AFA stainless steels. Upon reaching the desired temperature, the weighted loading tray was hooked on the wire cable attachment loop and the system put into tension. When the loading tray stabilized within a few seconds, the data record button on the data logger would be pressed to begin data logging. Temperature was held constant in each test.

At 760°C and under a 35 MPa load, it was established that the model alloy tested would enter the secondary creep regime approximately one hour after the specimen was put into tension by loading. It would remain at a steady state for at least a 1000 h duration (the longest duration tested). To capture a representative sample of the creep curve, the duration of each test was 500 h, with the exception of two shorter partial tests conducted to evaluate microstructural changes at stages on the creep curve.

Upon completion of a test, data recording would be terminated, the system unloaded and the furnace ramped down to room temperature. The test specimen would then be removed from the specimen grips and sectioned into three parts using a diamond saw as described in section 3.2.2. Figure 3.3 shows the locations of where the head, gauge and gauge-lengthwise sections were located along the T-bone specimens. These three locations were chosen to explore any differences in precipitate directionality or observable microstructural differences between the three sections.

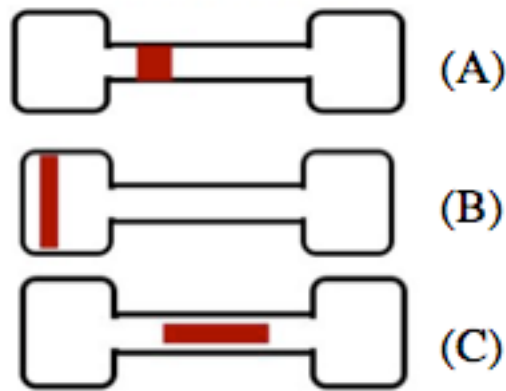


*Figure 3.3: Diagram detailing the locations of sections taken for SEM microstructural analysis from creep T-bones. (A) Gauge (B) Head (C) Gauge-lengthwise*

Creep curves of percent strain versus time were produced from the load and displacement data collected. Each crept sample was mounted, polished and imaged using scanning electron microscopy as detailed in section 3.3.1.

#### 3.4.2 Creep Test Experiments Performed

Elevated temperature constant-stress creep tests were conducted for a duration of 500 h for each aging condition at 760°C under a 35 MPa load. Each 500 h test was completed twice for each aging condition. Two partial constant-stress creep tests were conducted to evaluate the alloy's microstructural changes as it crept over time. Similar test conditions as the full range 500 h creep tests were used for the partial tests. Two specimens were homogenized at 1250°C but not aged. The first test was run for 3.5 h and the second test was stopped after 300 h duration to get representative samples along the creep curve. Samples were mounted, polished and imaged in the SEM after the creep

tests were complete and creep curves of strain percent over time were produced from the load and displacement data collected.

### 3.5 Tensile Tests

Flat T-bone test specimens approximately 1 mm thick, with a gauge length of 15 mm, and width of 2 mm were milled with the dimensions shown in Figure 3.4 from the Fe-20Cr-30Ni-2Nb-5Al model alloy as detailed in the materials preparation section 3.2.2. Each specimen was homogenized at 1250°C for 24 h and then aged at 760°C for 0, 2.4, 24 or 240 h. Specimens were polished on a turntable using successively finer silicon carbide abrasive paper up to 1200-grit, then with 0.3  $\mu\text{m}$  alumina powder dissolved in water.

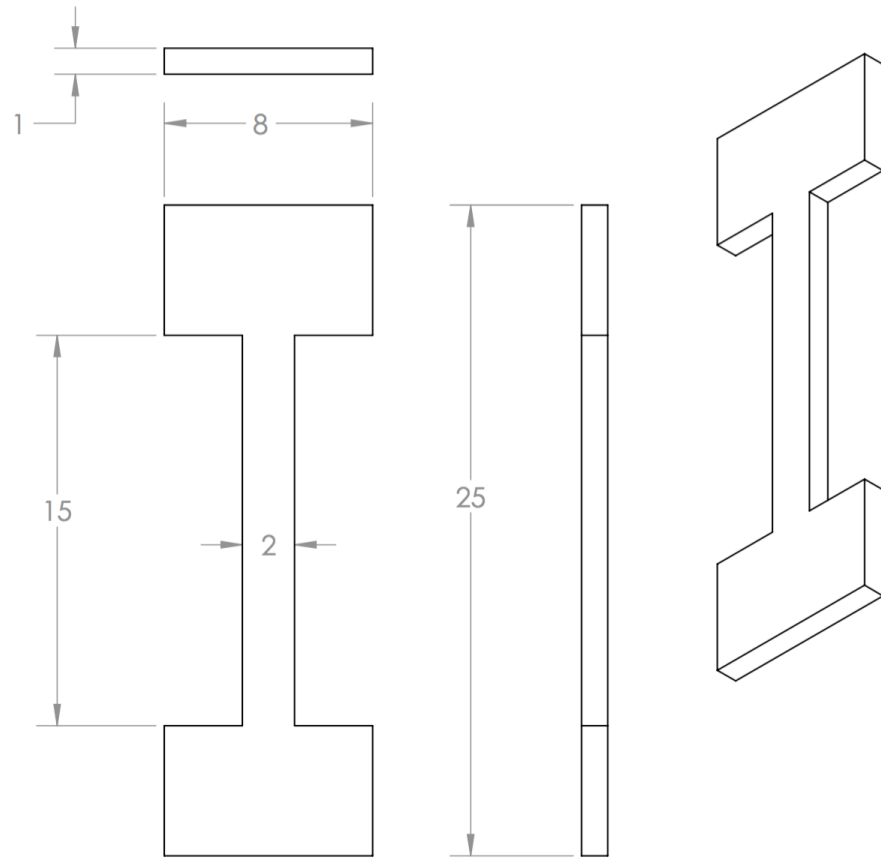


*Figure 3.4: Dimensions of tensile test specimen in millimeters.*

Samples were inserted into high-temperature specimen grips of the Instron 5690 tensile testing machine coupled with a MTS hydraulic testing machine. The metal frame of the Instron supports the Mellen Inc. SCR Split Series 120 V 1200 W Furnace mounted vertically. The furnace utilizes clamshell-heating elements capable of 1250°C in air. The temperature was measured with a centrally located K-type thermocouple and controlled by a Mellen Inc. PS105 programmable power control cabinet.

Elevated temperature tensile tests were conducted at 760°C with an applied preload force of 50 N. For all tests the initial strain rate was  $5 \times 10^{-4} \text{ s}^{-1}$ , and up to five

tensile tests were performed for each heat treatment protocol. To decrease the number of repeat tests that had to be performed, a soft mallet was used to secure the T-bones in the high temperature grips.

True strain ( $\epsilon$ ) and true stress ( $\sigma$ ) were calculated from the load-displacement data and reported as true stress-strain curves. The yield strengths and ultimate tensile strengths were recorded. Percent elongation of the specimen was obtained by comparing the initial specimen gauge length and measuring the specimen gauge length after the tests were completed using an optical microscope. To examine the fracture surface, samples were prepared and imaged using scanning electron microscopy as detailed in section 3.3.1.

# **CHAPTER 4        EFFECT OF AGING TIME ON**

## **MICROSTRUCTURE AND HIGH TEMPERATURE TENSILE AND**

## **CONSTANT-STRESS CREEP BEHAVIOR OF THE ALUMINA-**

## **FORMING AUSTENITIC STAINLESS STEEL Fe-20Cr-30Ni-2Nb-5Al**

### **4.1     Introduction**

In this chapter, the effects of aging time on the microstructure and high temperature creep and tensile behavior of the alumina-forming austenitic stainless steel model alloy Fe-20Cr-30Ni-2Nb-5Al (at.%) is investigated. High temperature tensile tests were performed and compared to room temperature results. Constant-stress creep tests were performed at an elevated temperature and the microstructure analyzed before and after each creep test. Additionally, the effect of aging temperature on the presence of precipitates in the alloy's matrix was explored.

### **4.2     Experimental**

Bright-field TEM was used to investigate the effect of aging temperature on the presence of precipitates in the alloy's matrix, specifically on the presence of  $\gamma'$ -Ni<sub>3</sub>Al (L<sub>1</sub><sub>2</sub>) at 760°C as detailed in Chapter 3.

To explore the effects of aging time on the microstructure of the alloy, specimens were homogenized at 1250°C and then aged 0, 2.4, 24 or 240 h at 800°C. Microstructural analysis was performed on the specimens for each aging condition.

The area fraction of grain boundary Laves phase and NiAl precipitates (designated as  $\rho$ ) for Fe-20Cr-30Ni-2Nb-5Al (at. %) was quantitatively analyzed using equation (1)<sup>49</sup>, where  $l$  is the length of the grain boundary covered by Laves phase particles and NiAl precipitates and  $L$  is the total length of the grain boundary:

$$\rho(\%) = \frac{l_1 + l_2 + l_3 + l_4 + \dots}{L} \times 100 \quad (1)$$

The value of  $\rho$  was calculated from the average of three BSE images of mechanically polished samples where the value of  $L$  was approximately 0.8  $\mu\text{m}$  in each sample.

Elevated temperature tensile tests were conducted at 760°C with an applied preload force of 50 N for specimens homogenized at 1250°C for 24 h and subsequently aged at 800°C for 0, 2.4, 24 or 240 h as described in Chapter 3. Up to five tensile tests were performed for each heat treatment protocol. See Chapter 3 for details on testing methods and microstructural characterization. SEM images of the sample fracture surface were taken after tensile testing was complete.

Constant-stress creep tests were performed under a 35 MPa load at an elevated temperature of 760°C for specimens homogenized at 1250°C and then aged 0, 2.4, 24 or 240 h at 800°C. At least two 500 h tests were completed for each aging condition. To gain insights into strain rate behavior at longer time intervals, creep tests were conducted for aging conditions of 2.4 h, 24 h and 240 h and lasting for durations of 1000 h, 750 h and 800 h respectively.

To study the effect of temperature on creep rate, two constant-stress creep tests were performed on homogenized specimens under a 35 MPa load at elevated temperatures of 760°C and 700°C.

To explore the effects of straining at an elevated temperature on the microstructure of the alloy, microstructural analysis was performed on the specimens for each aging condition after the completion of a 500 h creep test. Images were taken of three locations along each T-bone for each condition.

### 4.3 Results and Discussion

#### 4.3.1 Investigating presence of $\gamma'$ -Ni<sub>3</sub>Al (L1<sub>2</sub>) precipitates at 760°C

A bright-field TEM image of a precipitate located on the edge of a thin foil in a sample of Fe-20Cr-30Ni-2Nb-5Al (at. %) homogenized at 1250°C for 24 h, aged at 800°C for 24 h and crept for ~800 h at 760°C is shown in Figure 4.1 (a). A selected area diffraction pattern (SADP) taken from the f.c.c. matrix is shown in Figure 4.1 (b). The strong diffraction spots are from the L1<sub>2</sub> phase  $\gamma'$ -Ni<sub>3</sub>Al precipitate superlattice reflections, and the orientation relationship between the f.c.c. austenite matrix and the L1<sub>2</sub> phase is cube-on-cube, mimicking results of alloys with similar compositions to Fe-20Cr-30Ni-2Nb-5Al (at. %) that have exhibited L1<sub>2</sub>  $\gamma'$ -Ni<sub>3</sub>Al precipitates <sup>19,34,50</sup>. This result confirms that this precipitate is the  $\gamma'$ -Ni<sub>3</sub>Al L1<sub>2</sub> phase.

In prior studies on Fe-19Cr-2.5Al-32Ni-3.3Nb, an alloy with a related composition to the model alloy, the presence of  $\gamma'$ -Ni<sub>3</sub>Al was found after creep-rupture tests conducted at 750°C and under a 100 MPa load and were said to improve the alloy's

creep properties<sup>20</sup>. However, the precipitate was not found after annealing at 800°C in an alloy of the same composition as the model alloy used here<sup>35</sup>. The current result confirms the presence of the  $\gamma'$ -Ni<sub>3</sub>Al precipitate at 760°C, thus extending the upper bound temperature at which  $\gamma'$ -Ni<sub>3</sub>Al has been found to be stable. Further work needs to be conducted to determine the temperature at which Ni<sub>3</sub>Al particles are no longer stable.

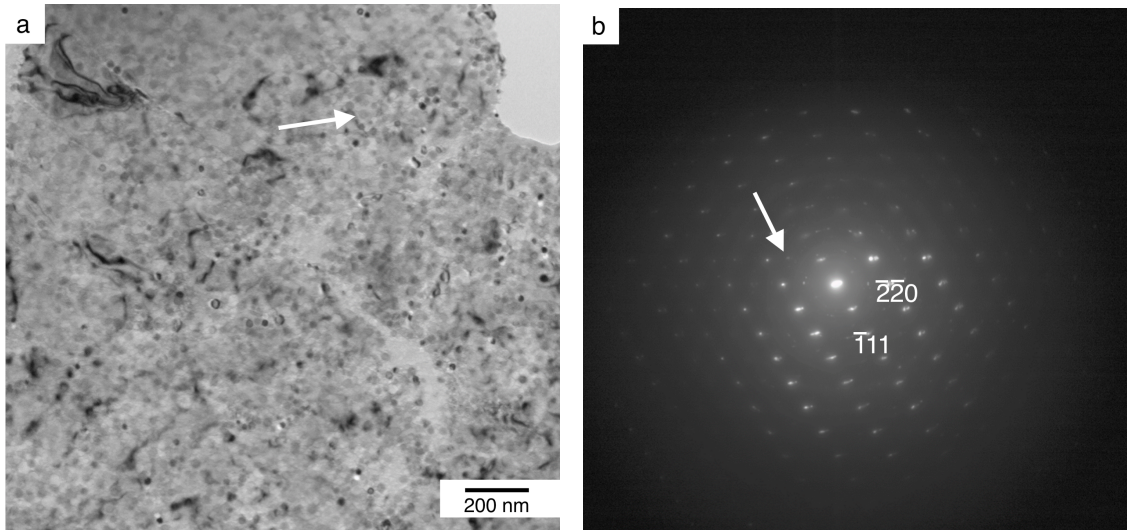


Figure 4.1: (a) Bright-field TEM image of Fe-20Cr-30Ni-2Nb-5Al (at. %) homogenized at 1250°C for 24 h, aged at 800°C for 24 h and crept for ~800 h at 760°C with an arrow indicating the matrix; (b) corresponding selected area diffraction pattern of the matrix showing  $\gamma'$ -Ni<sub>3</sub>Al (L1<sub>2</sub>) superlattice reflections (arrowed). Courtesy of Margaret Wu.

#### 4.3.2 Characterizing the effects of aging time on the alloy's microstructure

Figure 4.2 shows BSE images of the microstructure evolution of Fe<sub>2</sub>Nb Laves phase precipitates after a homogenizing anneal at 1250°C for 24 h and subsequent aging

at 800°C for 2.4 h, 24 h, and 240 h. Fe<sub>2</sub>Nb Laves phase precipitates are common in AFAs<sup>10,13,16,18,19,51</sup>. It can be seen in Figure 4.2 (a) that after annealing at 1250°C, the alloy shows no precipitation in the single-phase f.c.c. matrix prior to aging. This is consistent with findings by Trotter et al.<sup>38</sup> who found no evidence of precipitation in the model alloy after a solutionizing anneal at the same temperature.<sup>52</sup>

After aging for 2.4 h (b), 24 h (c), and 240 h (d), the alloy exhibits increasing quantities of fine dispersions of lightly contrasted Fe<sub>2</sub>Nb Laves phase precipitates in the SEM images. After aging for 2.4 h, the Laves phase is present only on the grain boundaries, however after aging for 24 h and 240 h at 800°C, in addition to appearing on the grain boundaries, the particles are also observed in the alloy's austenite matrix. The Laves phase precipitates along the grain boundaries are clearly coarser than those in the interior of the grains. In contrast to previous studies' findings where a few darkly contrasted B2-NiAl particles were found to accompany the Laves phase precipitation on the grain boundaries after a 2.4 h heat treatment and were larger than the Laves phase particles, growing at a faster rate and widespread throughout the matrix and on the grain boundaries after a 240 h anneal, no such precipitates appeared on the grain boundaries or in the matrix of the model alloy in this investigation even after the 240 h heat treatment.<sup>38,52</sup> One possible explanation for this difference may be the different stock alloys and the manufacturing methods used to fabricate each respective alloy. For this study, the stock alloy was cast into 8 kg ingots after a split-cast vacuum induction melt,

while the stock alloy used in the study by Trotter et al. was cast into significantly smaller 200 g ingots by vacuum arc-melting followed by drop casting into a copper crucible.

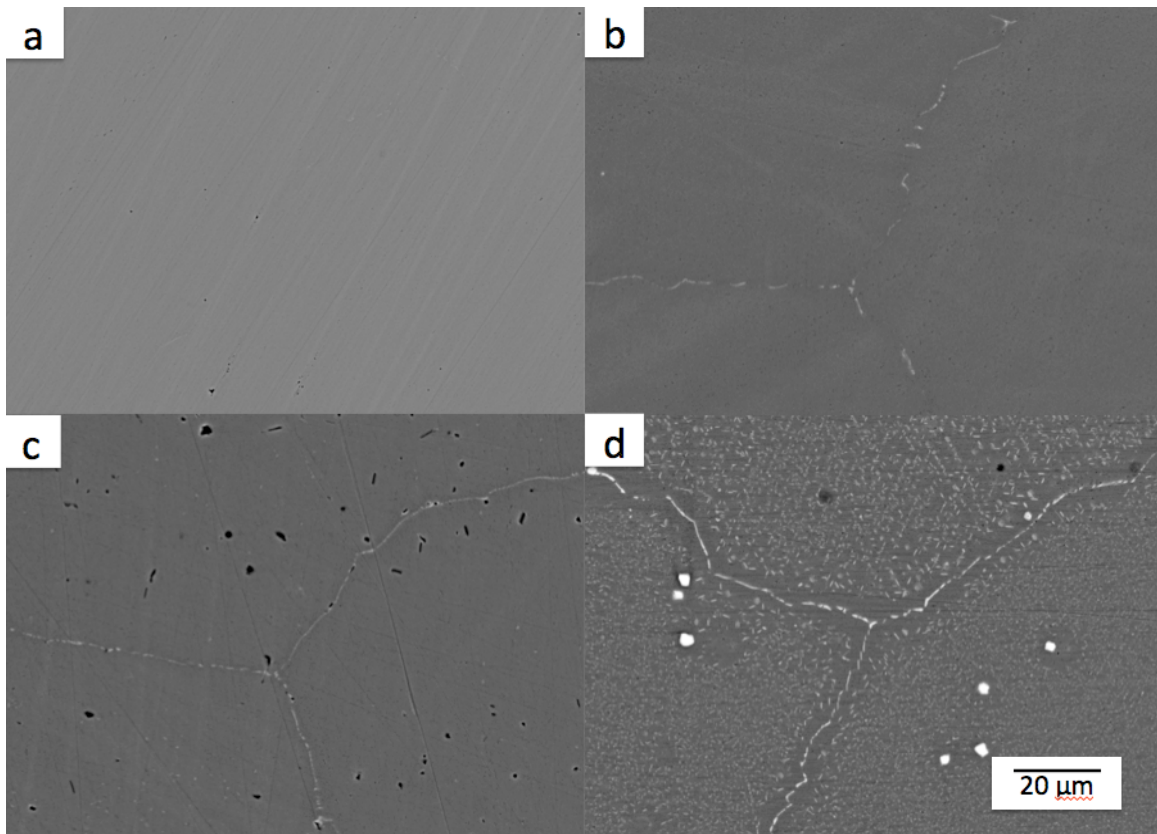


Figure 4.2: BSE SEM images of Fe-20Cr-30Ni-2Nb-5Al (at. %) homogenized at 1250°C for 24 h (a), then subsequently aged at 800°C for 2.4 h (b), 24 h (c), and 240 h (d). The light precipitates are the Laves phase.

Figure 4.2 (d) shows that after aging for 240 h, there is significant Laves phase precipitation in the matrix of the alloy and the precipitates have significantly increased in size when compared to shorter duration heat treatments. A precipitate-free zone (PFZ) is visible adjacent to the grain boundary in the sample aged for the longest duration. This is

similar to the formation of a PFZ in findings by Trotter et al., where it was noted that as aging time increased a PFZ became evident on the grain boundaries and increased in size. The presence of a PFZ in the aged samples is not surprising since the grain boundaries and matrix precipitates are made up of the same solute atoms, and a PFZ can arise either from a depletion of solute atoms proximal to the grain boundary, or from a depletion of lattice vacancies<sup>38,52,53</sup>. Images from a study on Fe-20Cr-30Ni-2Nb-5Al (at.%) that was creep tested at 750°C under a 100 MPa load, show a PFZ along the grain boundaries covered by alternating Fe<sub>2</sub>Nb and NiAl phase particles. It was hypothesized that this effect was due to the formation of NiAl on the grain boundary, which caused local Al depletion in the adjacent matrix, and that elimination of the PFZ may further improve the alloy's creep properties<sup>20</sup>.

Table 4.1 shows how the area fraction of grain boundary Fe<sub>2</sub>Nb Laves phase and NiAl precipitates changes with aging time. When the sample was fully solutionized at 1250°C but not heat treated, there is no grain boundary coverage and the alloy is single phase austenite. After a 2.4 h heat treatment at 800°C, the grain boundary area fraction is 42%. The grain boundary coverage is 69% for samples aged for 24 h and increases to 77% for samples aged 240 h. These grain boundary coverage values are consistent with the upward trend in increasing grain boundary coverage found in prior work on this model alloy by Trotter et al., shown adjacent to values found in this investigation in the right column of Table 4.1.<sup>38</sup> Net differences in grain boundary area fraction percentages

between this study and Trotter et al. can be attributed to different stock alloys and manufacturing techniques as described above.

*Table 4.1: Area fraction of grain boundary (GB) Laves phase for Fe-20Cr-30Ni-2Nb-5Al (at. %) homogenized at 1250°C and aged at 800°C for 0, 2.4, 24 or 240 h with results from this investigation in the left column and results from Trotter et al. in the right column. GB area fractions are calculated from an average of at least three BSE images for each aging condition.*

<b>Aging time (h)</b>	<b>GB area fraction (%)</b>	<b>GB area fraction (%) Trotter et al.</b>
0	0	0
2.4	42±2	56
24	68.5±5	78
240	77.2±4	84

#### 4.3.3 Effect of aging time on high temperature tensile behavior

To study the effect of aging time on the model alloy's high temperature tensile behavior, tensile tests were conducted at different aging conditions at an elevated temperature and the results were compared to room temperature tensile tests.

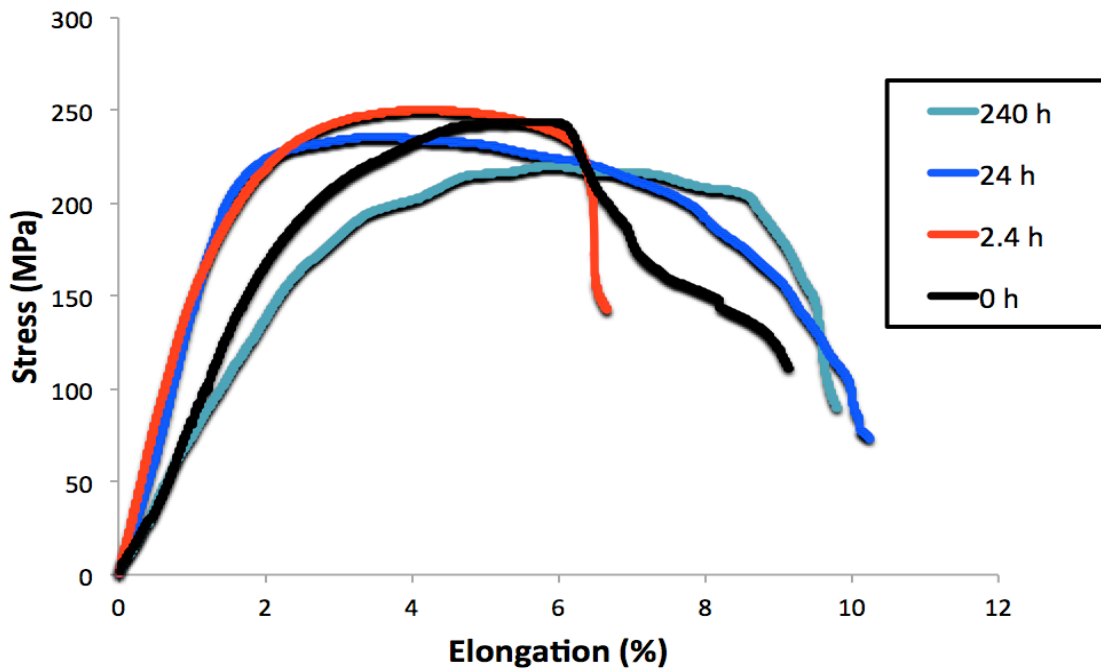


Figure 4.3: High temperature tensile curves of Fe-20Cr-30Ni-2Nb-5Al (at. %) homogenized at 1250°C for 24 h and subsequently aged at 800°C for 0, 2.4, 24 or 240 h as indicated. Tensile tests were conducted at 760°C with an initial strain rate of  $5 \times 10^{-4} \text{ s}^{-1}$ . Results are the average of at least three tests at each condition.

Figure 4.3 shows typical high temperature tensile curves of Fe-20Cr-30Ni-2Nb-5Al (at. %) conducted at 760°C with an initial strain rate of  $5 \times 10^{-4} \text{ s}^{-1}$ . Prior to tensile testing, samples were homogenized at 1250°C for 24 h and aged at 800°C for 0, 2.4, 24 or 240 h. At least three tests were conducted at each condition and the results averaged (see Appendix IV for high temperature tensile test curves for each aging condition).

Table 4.2 provides a summary comparison of high temperature and room temperature values for the average yield strength (YS), ultimate tensile strength (UTS), and

elongation to failure ( $\epsilon_f$ ) for Fe-20Cr-30Ni-2Nb-5Al (at. %) homogenized at 1250°C for 24 h, heat treated at 800°C and strained under tension with an initial strain rate of  $5 \times 10^{-4} \text{ s}^{-1}$ .

*Table 4.2: Yield strength (YS), ultimate tensile strength (UTS), and elongation to failure ( $\epsilon_f$ ) for Fe-20Cr-30Ni-2Nb-5Al (at. %) homogenized at 1250°C for 24 h, heat treated at 800°C and strained under tension at 760°C or at room temperature with an initial strain rate of  $5 \times 10^{-4} \text{ s}^{-1}$ . Results are the average of at least three tests at each condition. Room temperature data courtesy of Trotter et al.*

Aging time (h)	YS (MPa)	UTS (MPa)	$\epsilon_f$ (%)	YS (MPa)	UTS (MPa)	$\epsilon_f$ (%)
	760°C	760°C	760°C	20°C	20°C	20°C
0	188±5	249±19	7.7±1.6	205	338	52
2.4	225±7	252±24	5.7±1.2	322	502	37
24	202±7	236±15	8.9±0.5	362	707	29
240	166±11	224±9	9.6±1.4	351	715	28

As demonstrated in Table 4.2, the high temperature YS, UTS and elongations to failure were all significantly lower compared to results of tensile tests conducted at room temperature on the model alloy in prior studies<sup>38</sup>. For the 2.4 h aged sample no discontinuities were observed in the stress-strain curves - the 2.4 h aged room temperature tensile sample exhibited an upper and lower yield point and 5% Lüder's strain. Interestingly, the room temperature YS for the 2.4 h sample has the lowest value of all the heat treated samples (2.4 h, 24 h, 240 h), but has the highest value of all

samples tested, including the homogenized sample, for the high temperature tests. This may be attributed to the presence of fine L<sub>1</sub><sub>2</sub> precipitates pinning dislocations and strengthening the alloy. As the precipitates increase in size and coarsen, the strengthening effect decreases.

Elongations to failure were several times greater for tensile tests conducted at room temperature compared to those performed at 760°C. Whereas elongations continuously decreased with aging for room temperature tests, for high temperature tests, the elongation dipped two percentage points between the as-homogenized and 2.4 h aged sample and then steadily increased with aging time. The YS and UTS reached maximum values of 225-253 MPa for high temperature tests and 362-715 MPa for room temperature tests, respectively. The sample aged for 240 h exhibited the lowest yield strength at 760°C (166 MPa) of all the heat treatments tested, even when compared to the as-homogenized high temperature sample, which had a yield strength of 188 MPa. Figure 4.4 shows the fracture surface for Fe-20Cr-30Ni-2Nb-5Al (at. %) after being homogenized at 1250°C for 24 h, aged at 800°C for 240 h and tensile tested at 760°C. This shows that there was ductile dimple-type rupture as well as fracture occurring on a grain boundary.

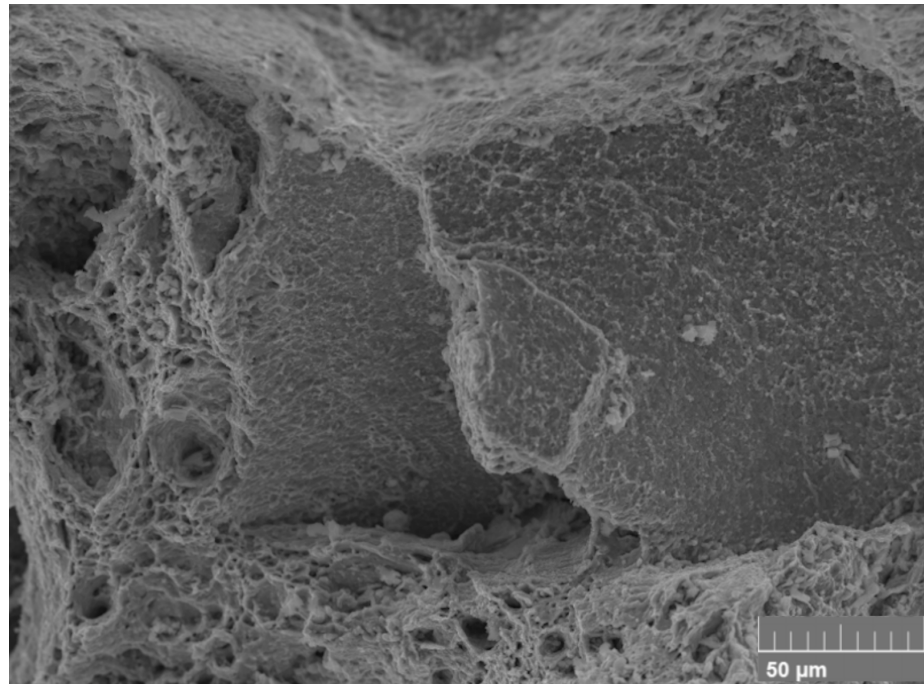


*Figure 4.4: BSE image of fracture surface for Fe-20Cr-30Ni-2Nb-5Al (at. %) after being homogenized at 1250°C for 24 h, aged at 800°C for 240 h and strained under tension at 760°C with an initial strain rate of  $5 \times 10^{-4} \text{ s}^{-1}$ .*

#### 4.3.4 Effect of aging time on constant-stress creep properties

The initial 5 h and full 500 h duration of constant-stress creep curves conducted at 760°C and 35 MPa in air for Fe-20Cr-30Ni-2Nb-5Al (at. %) are shown in Figures 4.5 and Figure 4.6, respectively. Prior to creep testing, each specimen was homogenized at 1250°C for 24 h and subsequently aged at 800°C for 0, 2.4, 24 or 240 h. Two creep tests were performed for each aging protocol, and the creep curves for all replicates can be found in Appendix III. These creep test conditions were chosen for this investigation to

fall within the U.S. Department of Energy's goal for development of materials needed for the critical components of coal-fired boilers and turbines that are capable of operating with steam at temperatures of 760°C and pressures of 35 MPa<sup>7-9</sup>.

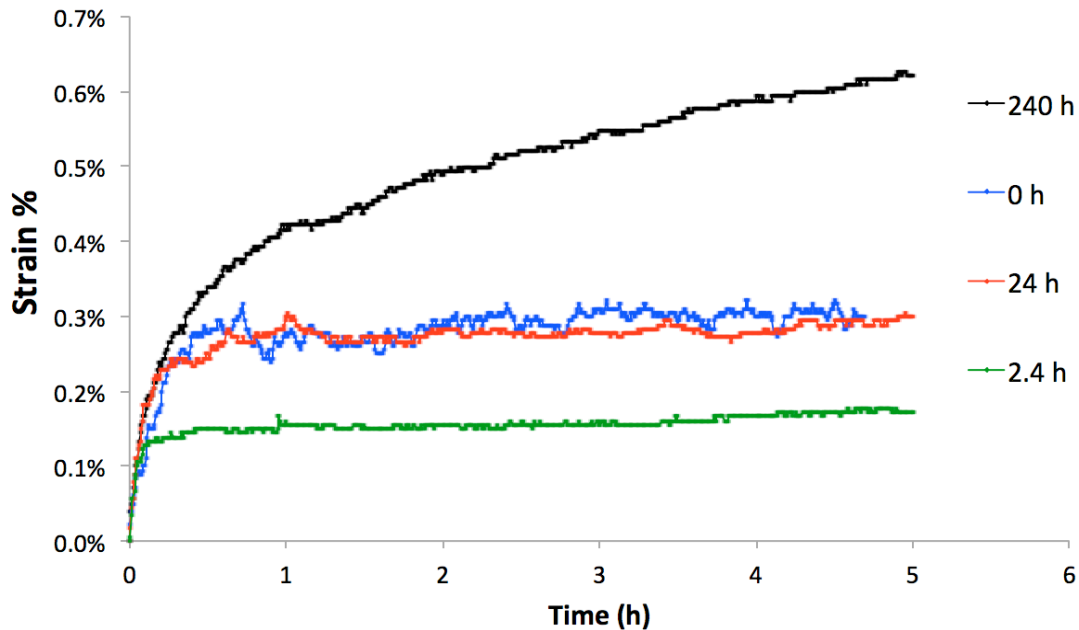
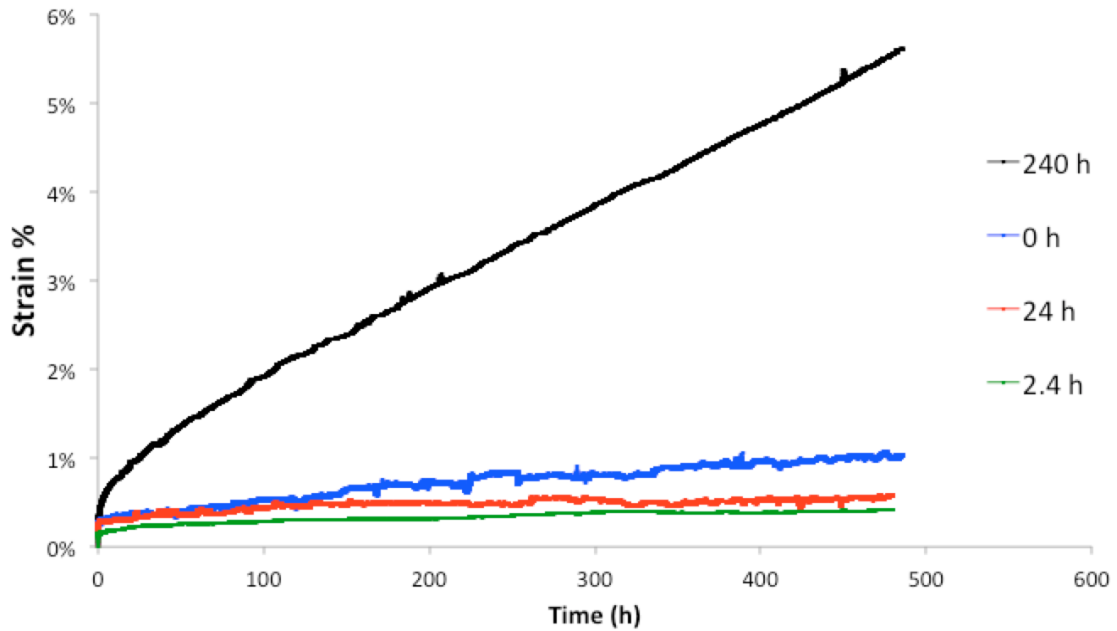


Figure 4.5: Initial five hours of constant-stress creep curves for Fe-20Cr-30Ni-2Nb-5Al (at. %) conducted at 760°C under a 35 MPa load in air. Specimens were homogenized at 1250°C for 24 h and subsequently aged at 800°C for 0, 2.4, 24 or 240 h prior to creep testing. Two creep tests were performed for each aging protocol.



*Figure 4.6: Constant-stress creep curves for Fe-20Cr-30Ni-2Nb-5Al (at. %) conducted at 760°C for 500 h under a 35 MPa load in air. Specimens were homogenized at 1250°C for 24 h and subsequently aged at 800°C for 0, 2.4, 24 or 240 h prior to creep testing. Two creep tests were performed for each aging protocol.*

During the initial creep phase, the samples heat treated for 0 h and 24 h had similar primary creep rates, which were higher than the primary creep rate of the 2.4 h aged samples. However, they diverged in their secondary creep rate, with the homogenized samples exhibiting a significantly higher secondary creep rate and reaching 1.1% strain at the completion of the test, while the samples aged for 24 h only reached 0.6% strain. This result is contrary to that found in prior creep studies on this alloy, which found lower creep rates for the homogenized material when compared to aged

specimens,<sup>20</sup> and contrary to the theory that the NiAl and Laves phase don't show strong precipitation hardening at high temperatures and therefore don't contribute to the creep strength<sup>54,55</sup>.

The primary creep strain correlates well with the high temperature yield strengths of the alloy (Table 4.2), with samples with higher creep strain correlating with lower yield strengths. The 240 h aged specimen had the highest primary creep strain and the lowest yield strength (166 MPa), while the 2.4 h specimen had the lowest primary creep strain and the highest yield strength (224 MPa). This result is in contrast to prior work that found that the creep rate did not correlate well with the yield strength<sup>18,21,54</sup>.

The samples aged for 2.4 h exhibited a similar secondary creep rate to the 24 h aged samples, and the lower overall strain of 0.4%, compared to the 24 h samples' 0.6%, can be attributed to the lower primary creep rate. This was an unusual finding because the area fraction of grain boundary Laves phase and NiAl precipitates was significantly higher, 69% compared to 42 % for the 24 h and 2.4 h aged samples, respectively, and the size of the precipitates was also significantly larger. The samples aged for 240 h exhibited the highest primary and secondary creep rates with an overall strain reaching 5.6% after 500 h of undergoing creep testing. This result was unsurprising given the 77% grain boundary coverage and large size of coarsened Laves phase and NiAl precipitates evident in both the matrix and along the specimen's grain boundaries.

Strain rate as a function of strain percent is plotted in Figure 4.7 for the constant-stress creep tests conducted for each aging condition. As is evident, strain rates remained

steady for the four aging conditions. The higher strain rates at the beginning of the creep tests for all samples tested can be attributed to the strain that occurs during the initial primary creep stage. The 240 h sample exhibited the highest steady strain rate, followed by the homogenized sample. The 24 h sample had a higher initial strain rate compared to the 2.4 h sample, but the two samples had an almost identical steady strain rate.

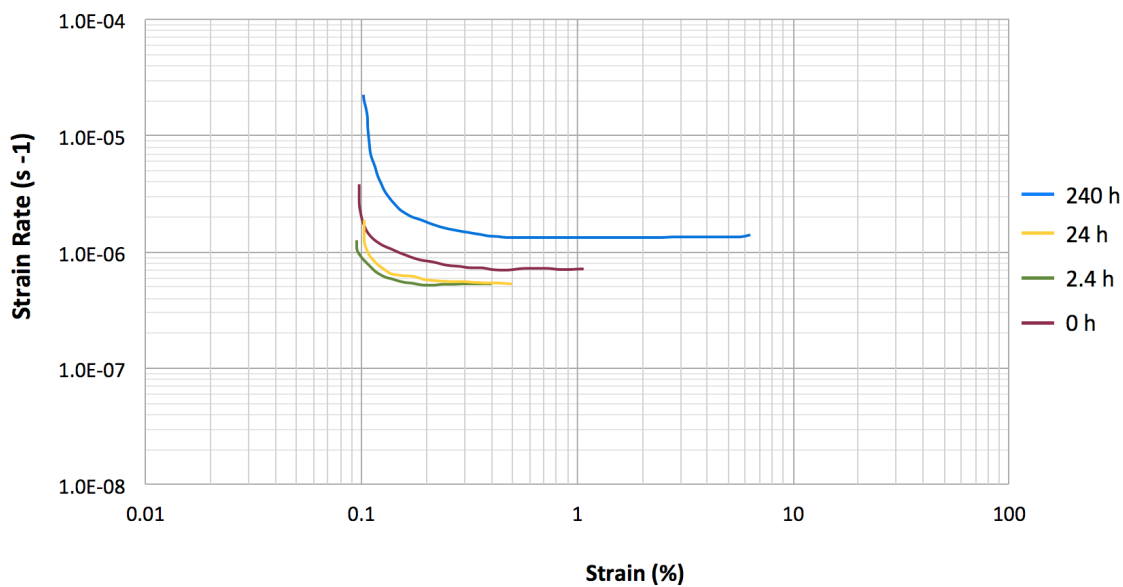
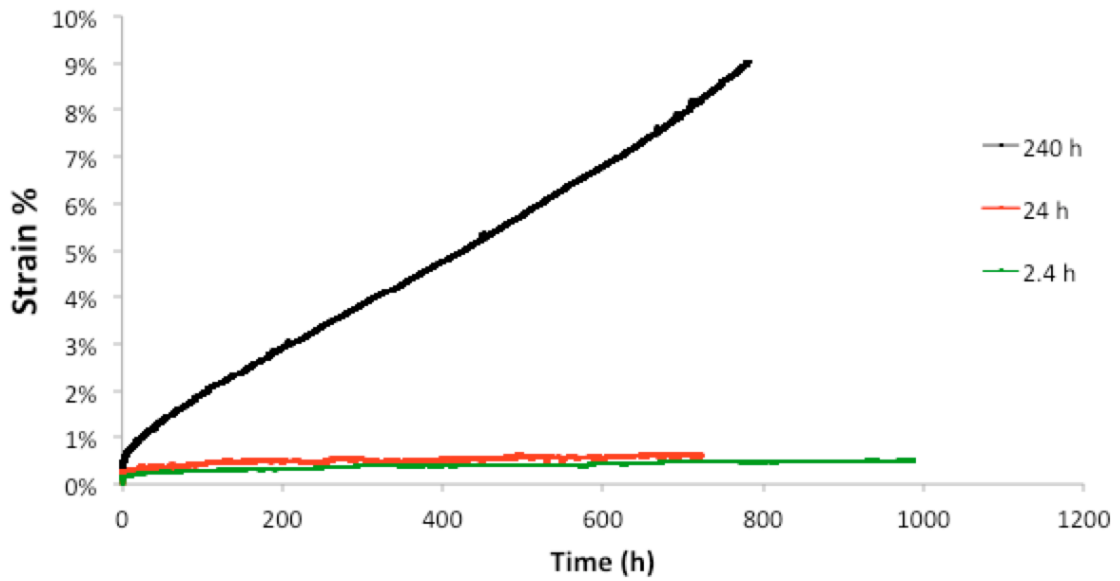


Figure 4.7: Strain rate as a function of strain are plotted for Fe-20Cr-30Ni-2Nb-5Al (at. %) conducted at 760°C for 500 h under a 35 MPa load in air. Specimens were homogenized at 1250°C for 24 h and subsequently aged at 800°C for 0, 2.4, 24 or 240 h prior to creep testing.

Overall, the creep rates correlate well with the measured high temperature yield strengths of the alloy as summarized in Table 4.2, with faster creep rates correlating with

lower yield strengths. This result is again in contrast to prior work that found that the creep rate did not correlate well with the yield strength<sup>18,21,54</sup>.

To begin investigating the alloy's long-term creep properties, three constant-stress creep tests were conducted at 760°C and 35 MPa in air for Fe-20Cr-30Ni-2Nb-5Al (at. %) for durations above 500 h, and the resulting creep curves are shown in Figure 4.8. Prior to creep testing, each specimen was homogenized at 1250°C for 24 h and subsequently aged at 800°C for 2.4, 24 or 240 h.



*Figure 4.8: Long-term constant-stress creep curves for Fe-20Cr-30Ni-2Nb-5Al (at. %) conducted at 760°C under a 35 MPa load in air for durations lasting longer than 500 h. Specimens were homogenized at 1250°C for 24 h and subsequently aged at 800°C for 2.4, 24 or 240 h prior to creep testing.*

The highest strain was reached by the sample aged for 240 h, with an overall strain of 9.1%. The trend of the 2.4 h and 24 h samples exhibiting a similar secondary creep rate, as seen for the first 500 h of the creep test, continued at longer time intervals of 720 h and 1000 h with the 24 h sample reaching 0.6% strain and the 2.4 h aged sample reaching a 0.5% strain, respectively. Further work on long-term creep tests and post-creep test microstructural analysis will be necessary to explore secondary creep properties and duration to creep-rupture.

#### *4.3.5 Effect of aging temperature on constant-stress creep rate*

To investigate how the alloy's creep rates changed with temperature, two constant-stress creep tests were conducted at 760°C and 700°C under a 35 MPa load and the resulting creep curves are shown in Figure 4.9. Prior to creep testing specimens were homogenized at 1250°C for 24 h but not heat treated.

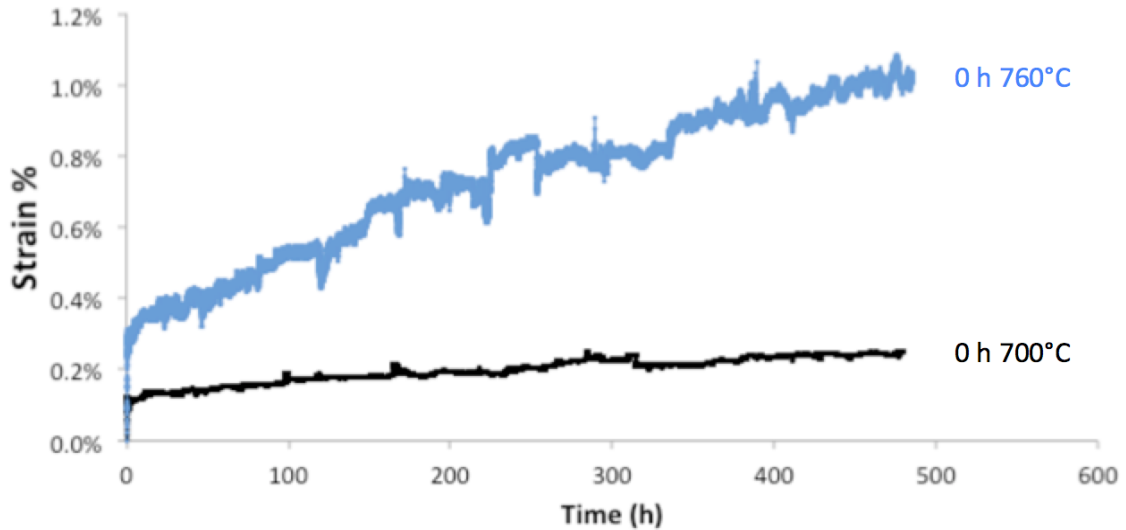


Figure 4.9: Constant-stress creep curves for Fe-20Cr-30Ni-2Nb-5Al (at. %) as-homogenized at 1250°C for 24 h tested at either 760°C or 700°C under a 35 MPa load.

The specimen creep tested at 700°C exhibited a significantly lower strain compared to the specimen tested at 760°C, with strains of 0.2% and 1.1%, respectively. This is an expected result as creep rates are temperature dependent, with high creep rates correlating with higher test temperatures<sup>21,54,56</sup>. Creep rate investigations at temperatures above 760°C remain to be investigated in future work.

#### 4.3.6 Effect of aging time on post-creep test microstructure

Figure 4.10 shows BSE images of the microstructural evolution of the Fe<sub>2</sub>Nb Laves phase and NiAl precipitates after a homogenizing anneal at 1250°C for 24 h, subsequent aging at 800°C for 2.4 h, 24 h, or 240 h and creep at 760°C for 500 h under a load of 35 MPa. The light contrast particles are the Laves phase and the dark contrast particles are NiAl precipitates. It can be seen in Figure 4.2 (a) that after the

homogenization anneal there is no evident precipitation, and after the completion of the 500 h creep test at 760°C, the alloy exhibits fine dispersions of light contrast  $\text{Fe}_2\text{Nb}$  Laves phase and dark contrast NiAl precipitates in the austenite matrix and on the grain boundaries of the alloy. These two precipitates are commonly found in heat treated and strained AFAs<sup>10,42,43</sup>.

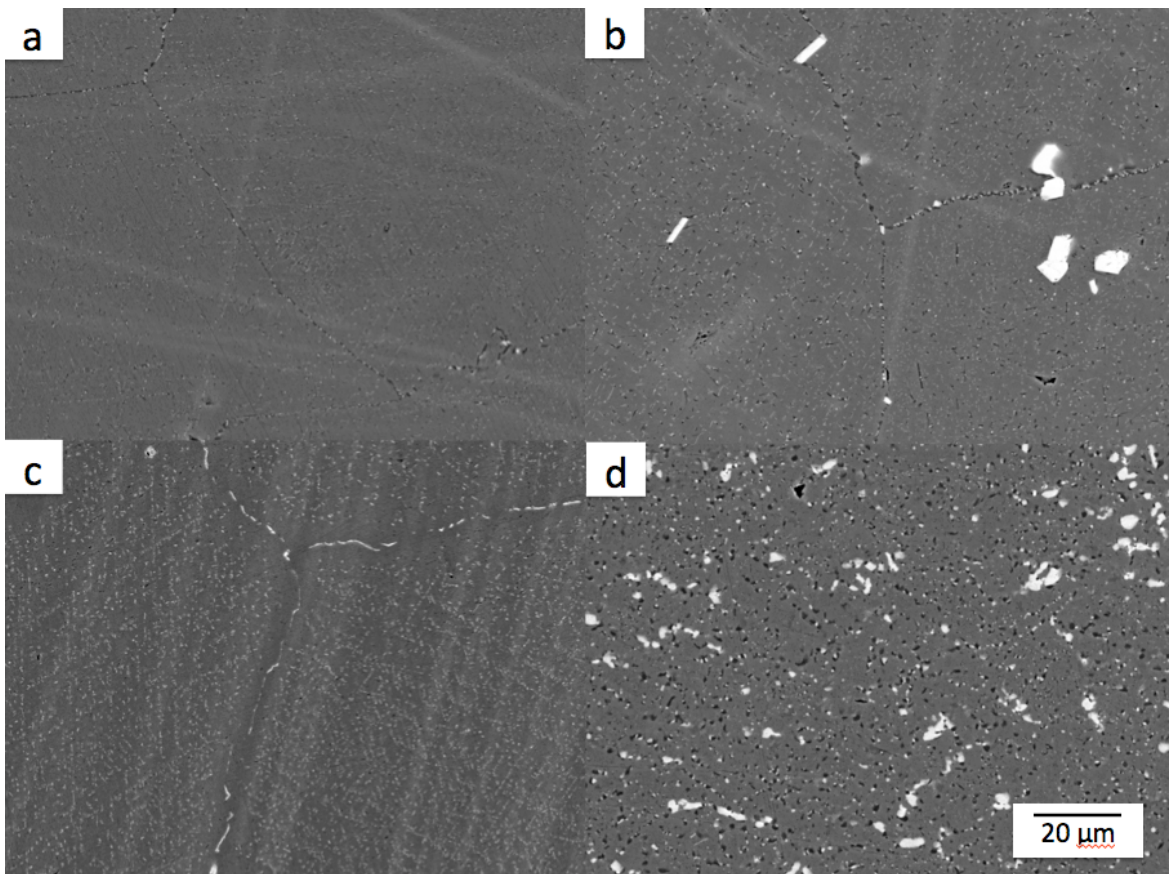


Figure 4.10: BSE images of Fe-20Cr-30Ni-2Nb-5Al (at. %) (a) homogenized at 1250°C for 24 h, then subsequently aged at 800°C for (b) 2.4 h, (c) 24 h and (d), 240 h and crept at 760°C for 500 h under a load of 35 MPa in air. The light precipitates are the Laves phase and the dark precipitates are NiAl precipitates.

As the aging time of the samples increases from 2.4 h (b) to 24 h (c) and then 240 h (d), the alloy exhibits increasing size and quantities of both the  $\text{Fe}_2\text{Nb}$  Laves phase and NiAl precipitates on the grain boundaries and in the matrix. The precipitates along the grain boundaries appear coarser than those in the interior of the grains in the matrix. A PFZ is visible adjacent to the grain boundary in the sample aged for 2.4 h, which becomes even more clearly visible in the sample aged for 24 h prior to creep. Figure 4.10 (d) shows that for the sample aged for 240 h and subsequently creep tested, there is significant Laves phase and NiAl precipitation in the matrix of the alloy and the precipitates have significantly increased in size compared to shorter duration heat treatments.

Comparing the images of samples heat treated for the same duration and taken prior to creep (Figure 4.2) to those imaged after creep testing was completed (Figure 4.10), it is evident that precipitation occurred during the 500 h long creep test. Table 4.3 compares the average grain boundary and matrix Laves and NiAl particle diameters and particle density of samples prior to and after creep testing was complete. Figure 4.11 shows side-by-side comparisons of magnified images taken prior to creep (left column) as compared to images taken after creep testing (right column) and are an example of the precipitate evolution that occurred in each sample tested.

*Table 4.3: Values prior to creep and after creep testing of average particle diameter and particle density for combined matrix and grain boundary Laves and NiAl precipitates for Fe-20Cr-30Ni-2Nb-5Al (at. %) homogenized at 1250°C for 24 h, then subsequently aged at 800°C for 2.4, 24 or 240 h and crept at 760°C for 500 h under a load of 35 MPa in air. Courtesy of Hailey Nicholson.*

Aging time (h)	Average Particle Diameter (nm)					
	Laves		NiAl		Particle Density (particles/μm^2)	
	Pre-creep	Post-creep	Pre-creep	Post-creep	Pre-creep	Post-creep
0	0	245±120	0	162±78	0.000	0.960
2.4	<100	352±194	0	236±110	<0.008	1.520
24	123±86	335±208	<100	303±190	0.282	1.680
240	163±113	520±334	<100	577±356	0.745	1.280

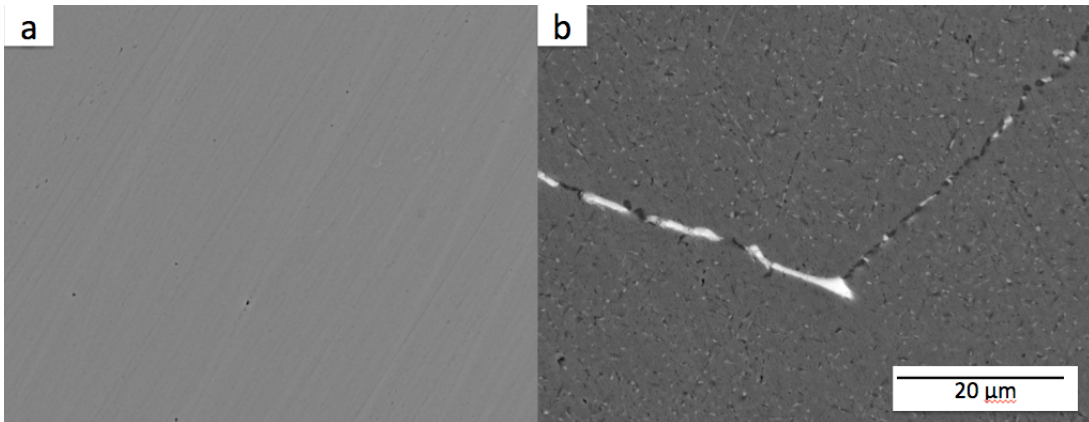


*Figure 4.11: BSE SEM images of Fe-20Cr-30Ni-2Nb-5Al (at. %) homogenized at 1250°C for 24 h prior to creep (a) and after creep testing (b). Constant-stress creep tests were conducted at 760°C for 500 h under a load of 35 MPa in air.*

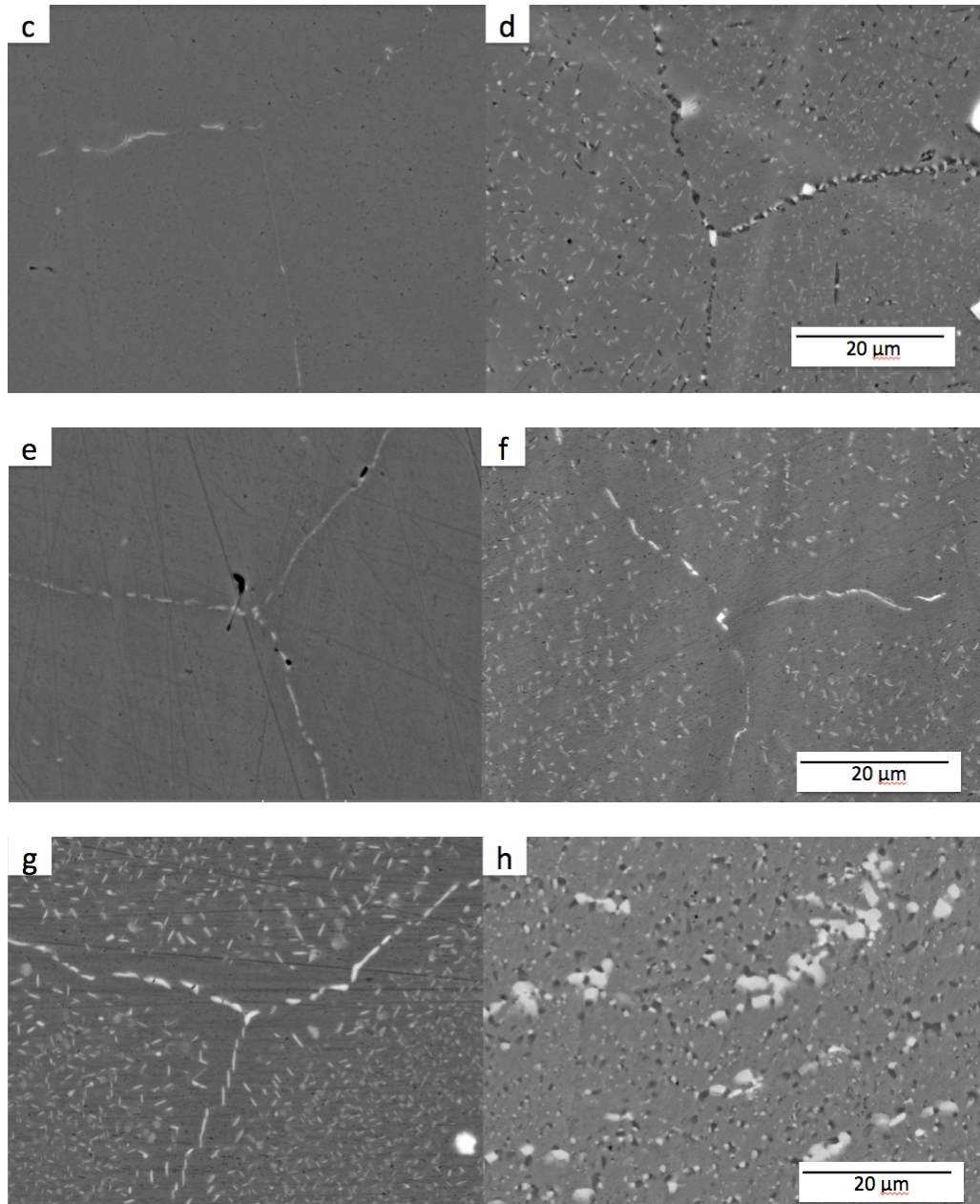


Figure 4.11: BSE images of Fe-20Cr-30Ni-2Nb-5Al (at. %) homogenized at 1250°C for 24 h and aged at 800°C for 2.4 h (c/d), 24 h (e/f) and 240 h (g/h) prior to creep/after creep testing respectively.

The density and size of precipitated Laves phase and NiAl particles increased for each aging condition throughout the duration of the creep tests of all specimens tested. As seen in Table 4.3, the average particle diameters and particle densities on the grain boundaries and in the matrix of the alloy were significantly higher post creep compared to pre-creep values for each respective aging condition. Particle size increased with aging time for both pre-creep and post-creep samples, reaching maximum values of 163 nm and 520 nm for Laves phase precipitates, respectively for the 240 h aged sample, with the post-creep's particle diameter having a value more than three times greater than the pre-creep value, demonstrating significant particle growth over the course of the creep test. Post-creep NiAl precipitates increased in size with increasing aging time, eventually catching up to and surpassing the Laves phase average particle diameter (520 nm) for samples aged 240 h (577 nm). These results mirrors those from Trotter et al., which found that with increasing aging time, particle diameters increased for matrix and grain boundary Laves and NiAl precipitates for Fe-20Cr-30Ni-2Nb-5Al (at. %) aged at 800°C, and that NiAl particle diameters eventually surpassed those measured of the Laves phase.<sup>38</sup> While the maximum pre-creep value for this investigation was 163 nm, Trotter et al. found that for an aging time of 240 h, the average particle diameter was 253 nm. This difference may be explained by the use of different stock alloys as discussed previously in this section.

Particle densities steadily increased with aging time for all pre-creep samples reaching a maximum of 0.745 particles/ $\mu\text{m}^2$  for the 240 h aged sample. In Table 4.4 it can

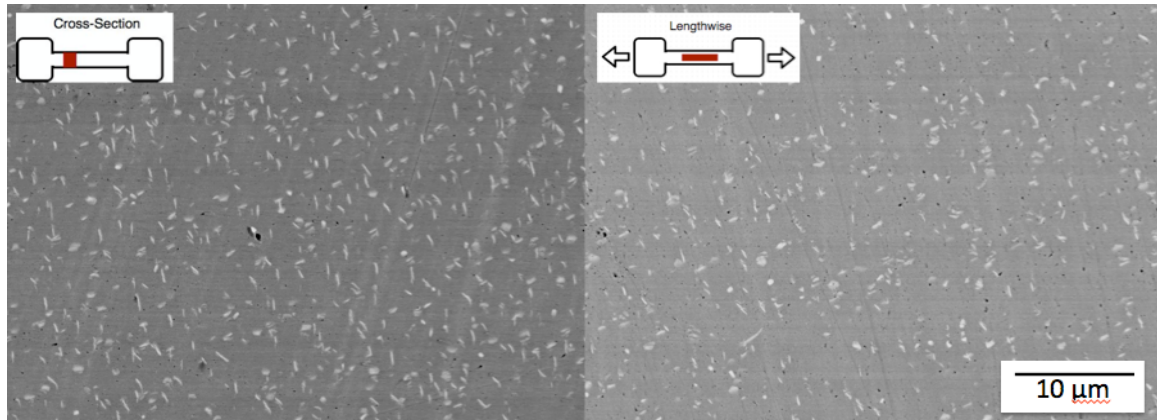
be seen that with increasing aging time the volume fraction of both Laves phase and NiAl precipitates increases, and that the volume fraction of samples post-creep is significantly higher compared to values prior to creep testing, suggesting that significant precipitation occurred during the creep testing process. For post-creep samples, particle densities increased for samples aged 0 h to 24 h to a maximum of 1.68 particles/ $\mu\text{m}^2$  and then dropped to 1.28 particles/ $\mu\text{m}^2$  for the 240 h aged sample. These results mirror the trend found by Trotter et al., where particle densities increased with aging time up to 24 h and a maximum value of 1.809 particles/ $\mu\text{m}^2$  and then dropped to 1.173 particles/ $\mu\text{m}^2$  for the sample aged for 240 h.<sup>38</sup> This drop in particle density may be explained by the coarsening and clumping of precipitates as the sample aged and crept. As precipitates increased in size, they took up more space both in the matrix and along grain boundaries and may have merged to form larger precipitate clumps instead of maintaining the fine dispersion of precipitates present in specimens aged for shorter durations.

*Table 4.4: Volume fraction and standard deviations for combined grain boundary and matrix NiAl and Laves phase particles for Fe-20Cr-30Ni-2Nb-5Al (at. %) homogenized at 1250°C for 24 h and aged at 800°C..*

<b>Aging time (h)</b>	<b>Laves</b>		<b>NiAl</b>	
	<b>Pre-creep</b>	<b>Post-creep</b>	<b>Pre-creep</b>	<b>Post-creep</b>
0	0	0.7±0.4	0	0.5±0.2
2.4	<0.1	1.7±0.9	0	1.1±0.5
24	0.1±0.1	2.8±1.1	<0.1	1.6±1.0
240	0.4±0.3	3.1±1.3	<0.1	2.3±1.4

In the samples imaged prior to creep testing, NiAl precipitates were either completely absent or few in number compared to the  $\text{Fe}_2\text{Nb}$  Laves phase (Figure 4.2). This is in contrast to the images taken after creep testing, where NiAl precipitates were present in every specimen, including the sample that was fully solutionized prior to creep and exhibited no visible signs of precipitation. These results are not surprising given that the creep testing temperature of  $760^\circ\text{C}$  was only  $40^\circ\text{C}$  lower than that of the heat treatment temperature of  $800^\circ\text{C}$ , so continued precipitation during the creep test was expected.

BSE images were taken at three locations along each T-bone for each post-creep microstructural analysis specimen in order to compare precipitation properties at a location where the sample was not strained (the head) and a location where the sample was strained (the gauge) as well as lengthwise along the gauge to determine if there were directional precipitation differences. Figure 4.12 shows that the precipitate structure in the cross-section of the gauge evolved in a similar way to the structure lengthwise along the gauge in images taken from the same crept T-bone sample.



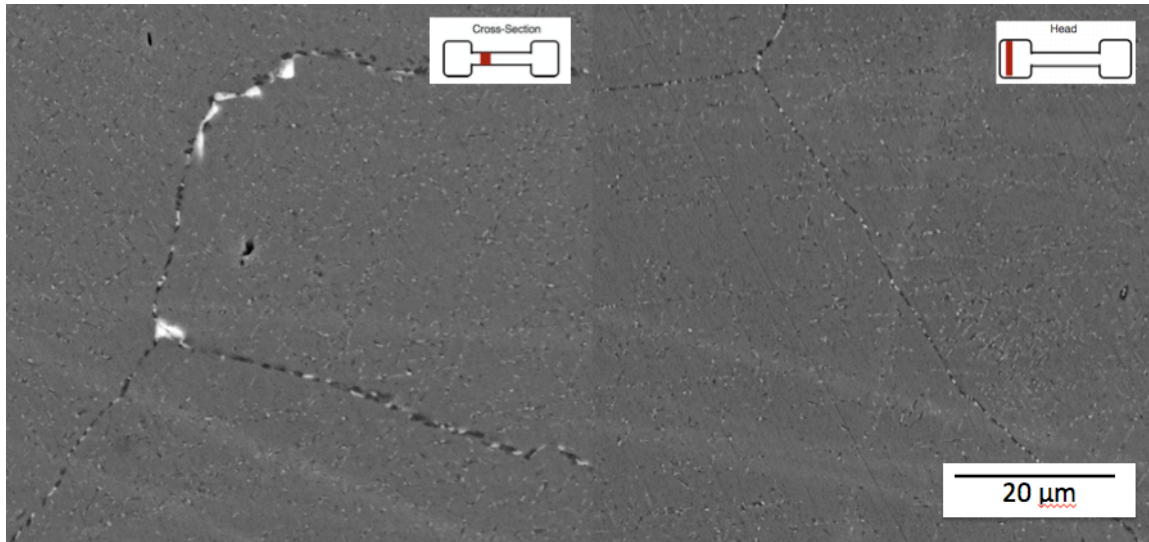
*Figure 4.12: BSE images of Fe-20Cr-30Ni-2Nb-5Al (at. %) homogenized at 1250°C for 24 h and subsequently aged at 800°C for 2.4 h and crept at 760°C for 500 h under a load of 35 MPa in air. Both images were taken from the gauge of the specimen with the left taken as a cross-section and the right lengthwise as indicated.*

Figure 4.13 shows a representative image taken from the gauge of a specimen (left), where the sample saw both the temperature and stress, and an image taken from the same T-bone sample's head (right) that saw only the temperature but not the strain. The precipitate structure of the gauge sample that had seen the stress of the creep test was significantly different from the smaller and less coarse precipitates found in the head of the T-bone sample that had only seen the same temperature but not the stress throughout the duration of the creep test. The data in Table 4.5 supports these findings, with a significant difference in particle diameter and particle density values between sample images taken from the head and gauge of the same crept T-bone sample. Samples taken from the gauge have an average particle diameter 100 nm greater than those values from the head, and particle density values in the gauge are over 0.4 particles/ $\mu\text{m}^2$  higher

compared to densities taken from images from the sample's head. It should be noted that it's possible that due to the vertical alignment of the specimen within the furnace, the temperature felt by the sample at the head and the gauge differed, contributing to the microstructure differences. Further investigation is needed to compare the microstructure of samples taken from opposite ends of a T-bone specimen; one sample from the head located higher in the furnace relative to the gauge and the other sample from the head located below.

*Table 4.5: Post-creep T-bone head and gauge comparison values of average Laves phase and NiAl particle diameter and particle density for Fe-20Cr-30Ni-2Nb-5Al (at. %) homogenized at 1250°C for 24 h and aged at 800°C for 240 h. Creep testing was conducted at 760°C for 500 h under a load of 35 MPa in air. Courtesy of Hailey Nicholson.*

Average Particle Diameter (nm)						
Aging time (h)	Laves		NiAl		Particle Density (particles/ $\mu\text{m}^2$ )	
	Head	Gauge	Head	Gauge	Head	Gauge
0	265±152	395±174	157±84	264±124	0.704	1.388
240	424±290	538±381	470±265	583±441	0.662	1.103



*Figure 4.13: BSE SEM images of Fe-20Cr-30Ni-2Nb-5Al (at. %) homogenized at 1250°C for 24 h and crept at 760°C for 500 h under a load of 35 MPa in air. The left image was taken from the gauge of the specimen with the left taken from the head as indicated.*

Overall, the precipitate structure evolved in a similar way in cross-sectional and lengthwise samples taken from the gauge, however samples taken from the head of the T-bone have significantly smaller average particle diameters and particle densities compared to the larger, more dense precipitates seen in samples taken from the gauge of the T-bone.

## CHAPTER 5      SUMMARY AND CONCLUSIONS

After annealing at 1250°C, Fe-20Cr-30Ni-2Nb-5Al (at. %) showed no precipitation in the single-phase f.c.c. matrix prior to aging. After aging for 2.4 h, 24 h, and 240 h, the alloy exhibited increasing quantities of fine dispersions of lightly contrasted  $\text{Fe}_2\text{Nb}$  Laves phase precipitates. After aging for just 2.4 h, the Laves phase was present only on the grain boundaries, however after aging for 24 h and 240 h at 800°C, the particles were also observed in the alloy's austenite matrix. The precipitates along the grain boundaries appeared coarser than those in the interior of the grains in the matrix. A precipitate-free zone (PFZ) was visible adjacent to the grain boundary in the sample aged for 240 h.

The  $\text{L1}_2$  phase  $\gamma'$ - $\text{Ni}_3\text{Al}$  precipitate was found at 760°C in a sample of Fe-20Cr-30Ni-2Nb-5Al (at. %) homogenized at 1250°C for 24 h, then aged at 800°C for 24 h and crept for ~800 h at 760°C. The presence of  $\text{L1}_2$  precipitates in aged samples could contribute to superior creep properties as the fine particles pin dislocations. Prior to this finding  $\gamma'$ - $\text{Ni}_3\text{Al}$  had only been found at 750°C and was not found at 800°C in an alloy of the same composition.

The area fraction of grain boundary  $\text{Fe}_2\text{Nb}$  Laves phase and  $\text{NiAl}$  precipitates increased with aging time. When the sample was fully solutionized at 1250°C, there was no grain boundary coverage. After aging for 2.4 h at 800°C, the grain boundary area fraction increased to 42%. The grain boundary coverage was 69% for samples aged for 24 h and increased to 77% for samples aged 240 h.

The high temperature YS, UTS and elongations to failure from tensile tests conducted at 760°C were significantly lower when compared to those from tests conducted at room temperature. The room temperature YS for the 2.4 h sample had the lowest value of all the heat treated samples (2.4 h, 24 h, 240 h), but had the highest value of all samples tested for the tests conducted at 760°C. The sample aged for 240 h exhibited the lowest yield strength of all the heat treatments tested. The primary creep strain correlated well with the high temperature yield strengths of the alloy, with samples with higher creep strain correlating with lower yield strengths.

The particle diameters and particle densities of precipitated  $\text{Fe}_2\text{Nb}$  Laves phase and NiAl precipitate particles increased for each aging condition when images taken prior to creep were compared to images taken after the completion of the 500 h constant-stress creep tests. Particle size increased with aging time for both pre-creep and post-creep samples, reaching maximum values of 163 nm and 546 nm, respectively. Particle densities increased with aging time up to 24 h and subsequently decreased for samples aged 240 h.

The precipitate structure evolved in a similar way in cross-sectional and lengthwise samples taken from the gauge of each crept sample, but samples taken from the head of the T-bone, which did not see the same stress as the gauge, had significantly smaller and less dense precipitates compared to the larger and more dense precipitates seen in samples taken from the gauge of the T-bone that had been exposed to the temperature and stress of the creep test.

Specimens heat treated for 0 h and 24 h had similar primary creep rates, which were higher than the primary creep rate of the 2.4 h aged samples. However, they diverged in their secondary creep rate, with the homogenized samples exhibiting a significantly higher secondary creep rate and reaching 1.1% strain at the completion of the test, while the samples aged for 24 h only reached 0.6% strain. Samples aged for 2.4 h exhibited a similar secondary creep rate to the 24 h aged samples. Samples aged for 240 h exhibited the highest primary and secondary creep rates with an overall strain of 5.6%.

High temperature creep rates correlated well with high temperature yield strengths of the alloy, with faster creep rates correlating with lower yield strengths.

The 700°C creep test exhibited a significantly lower creep rate compared to the 760°C creep test, with strains of 0.2% and 1.1%, respectively.

Overall, the alloy's creep resistance increased with sample aging time up to 24 h compared to as-homogenized samples. Fine dispersions of both Laves phase and NiAl precipitates characterized the microstructure of samples aged for 2.4 h and 24 h, with particle diameters not exceeding 350 nm. When the sample aging time was increased to 240 h, both the Laves phase and NiAl precipitates grew to diameters over 500 nm, and the volume fraction of both types of precipitates significantly increased. The creep strength of the 240 h aged alloy decreased and was significantly worse when compared to as-homogenized specimens and those aged for shorter durations. These results are similar to findings by Tarigan et al., which showed that a decrease in the precipitate size allows for dislocation pinning and leads to an increase in the alloy's creep strength. Smaller

average particle diameters at or around 350 nm in size and higher particle densities for both Laves phase and NiAl precipitates should therefore be targeted to promote superior long-term creep properties in the alloy. For all aging conditions, the microstructure continued to evolve after undergoing heat treatment throughout the duration of high temperature creep tests, signifying a need to investigate the development of alloys that can withstand the microstructural changes associated with aging for long durations at high temperatures and under load.

To summarize:

- The L1<sub>2</sub> phase  $\gamma'$ -Ni<sub>3</sub>Al precipitate was found at 760°C in the model alloy.
- The primary creep strain correlated well with the high temperature yield strengths of the alloy, with samples with higher creep strain correlating with lower yield strengths.
- The area fraction of grain boundary Fe<sub>2</sub>Nb Laves phase and NiAl precipitates increased with aging time.
- Particle size increased with aging time for both pre-creep and post-creep samples

## CHAPTER 6 FUTURE WORK

Future work should be divided amongst several focus areas:

1. Although three longer-term constant-stress creep tests were conducted for durations above 500 h, further investigations into the Fe-20Cr-30Ni-2Nb-5Al (at. %) alloy's short and long-term duration creep rates and post-creep microstructural analysis is necessary to explore secondary creep properties and time to creep-rupture.
2.  $\text{Ni}_3\text{Al}$  L1<sub>2</sub> particles were found in TEM images taken of samples crept at 700-760°C, but the upper temperature bound at which  $\text{Ni}_3\text{Al}$  remains stable and provides superior creep properties is yet to be determined. Additionally, in order to characterize how Fe-20Cr-30Ni-2Nb-5Al (at. %) performs at a range of high temperatures above 760°C and identify the effect of temperature on creep rates, further constant-stress creep tests at temperatures above 760°C should be performed and the presence of  $\text{Ni}_3\text{Al}$  investigated by imaging with TEM.
3. The addition of silicon to AFA stainless steels up to 0.3 wt. % has been shown to improve the formation of alumina scales and stimulate precipitation of NiAl, while helping to refine and stabilize  $\text{Fe}_2\text{Nb}$  Laves phase particles in Fe-20Cr-30Ni-2Nb alloys (at. %).<sup>57</sup> The effect of adding 0.2% silicon to Fe-20Cr-30Ni-2Nb-5Al (at. %) should therefore be studied to determine if NiAl precipitation is stimulated and how this addition affects the alloy's creep properties and microstructure. The same aging protocol used for

the non-silicon doped material should be administered and creep tests conducted at 760°C and 35 MPa in order to compare the obtained creep rates and characterized microstructure to those obtained in this investigation.

## APPENDICES

### Appendix I: Constant Stress Derivation

$$x = \frac{a}{1+b\theta} \left[ \cos(\theta) + \frac{b \sin(\theta)}{1+b\theta} \right] \quad (1)$$

$$y = \frac{a}{1+b\theta} \left[ \sin(\theta) - \frac{b \cos(\theta)}{1+b\theta} \right] \quad (2)$$

$$a = \frac{r_0 L_0}{L_0 - R\theta_0} \quad \text{and} \quad b = \frac{R}{L_0 - R\theta_0}$$

To maintain a constant stress, the following condition must be satisfied:

$$rL = \text{constant} = r_0 L_0 \quad (1)$$

Where:

$L_0$  = initial specimen length

$r_0$  = initial value of  $r$  (instantaneous moment arm of the applied weight)

The instantaneous specimen length can be written as:

$$L = L_0 + (\theta - \theta_0)R \quad (2)$$

Where:

$\theta_0$  = angle for initial positioning of constant-stress cam

Eliminating  $L$  from equations (1) and (2) gives you the equation

for the profile of a constant-stress cam:

$$r = \frac{r_0 L_0}{L_0 + R(\theta - \theta_0)} \quad (3)$$

This equation needs to be transformed into fixed a Cartesian coordinate system for ease of use in terms of  $x$  and  $y$ .

$$x = r \cos(\theta) + z \sin(\theta) \quad (4)$$

$$y = r \sin(\theta) - z \cos(\theta) \quad (5)$$

$$\frac{dx}{dy} = -\tan(\theta) \quad (6)$$

Eliminating  $x$  and  $y$  from the equations:

$$z = \frac{dr/d\theta}{\frac{r_0 L_0 R}{|L_0 + R(\theta - \theta_0)|^2}} \quad (7)$$

Substituting the above equation and equation (3) into equations (4) and (5)

yields the fixed coordinates of the constant-stress cam in terms

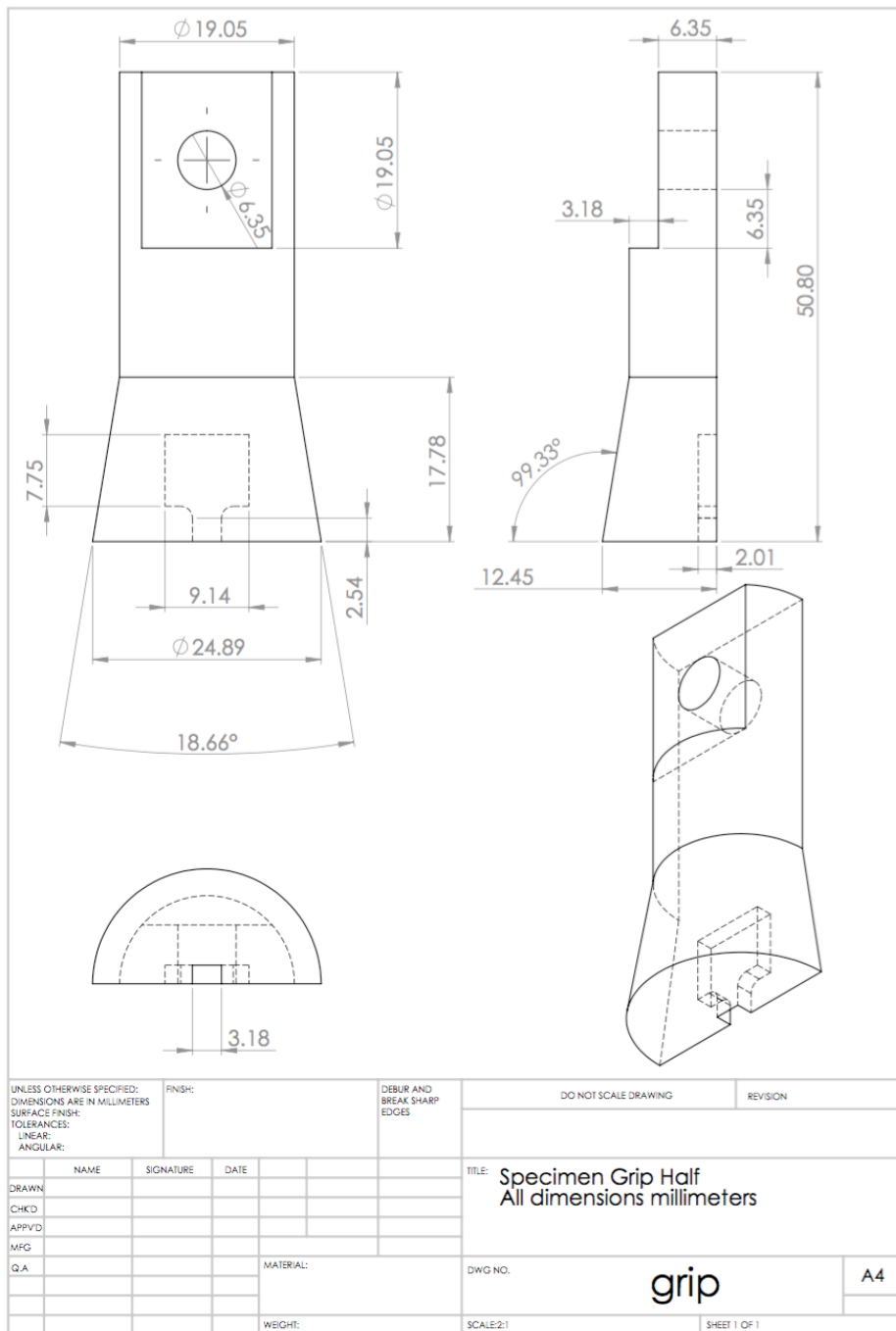
of the single parameter  $\theta$ :

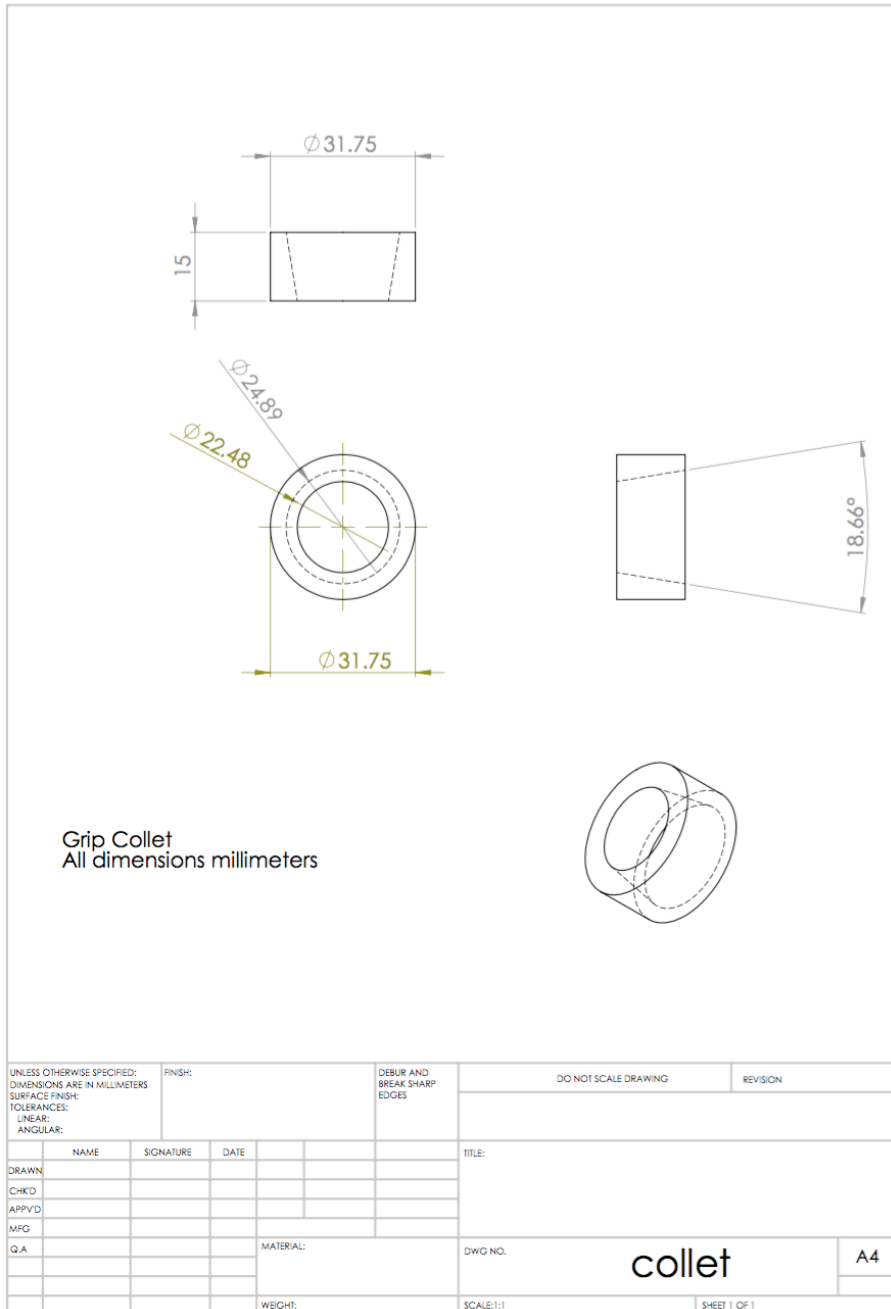
$$x = \frac{a}{1 + b\theta} \left[ \cos(\theta) + \frac{b \sin(\theta)}{1 + b\theta} \right] \quad (8)$$

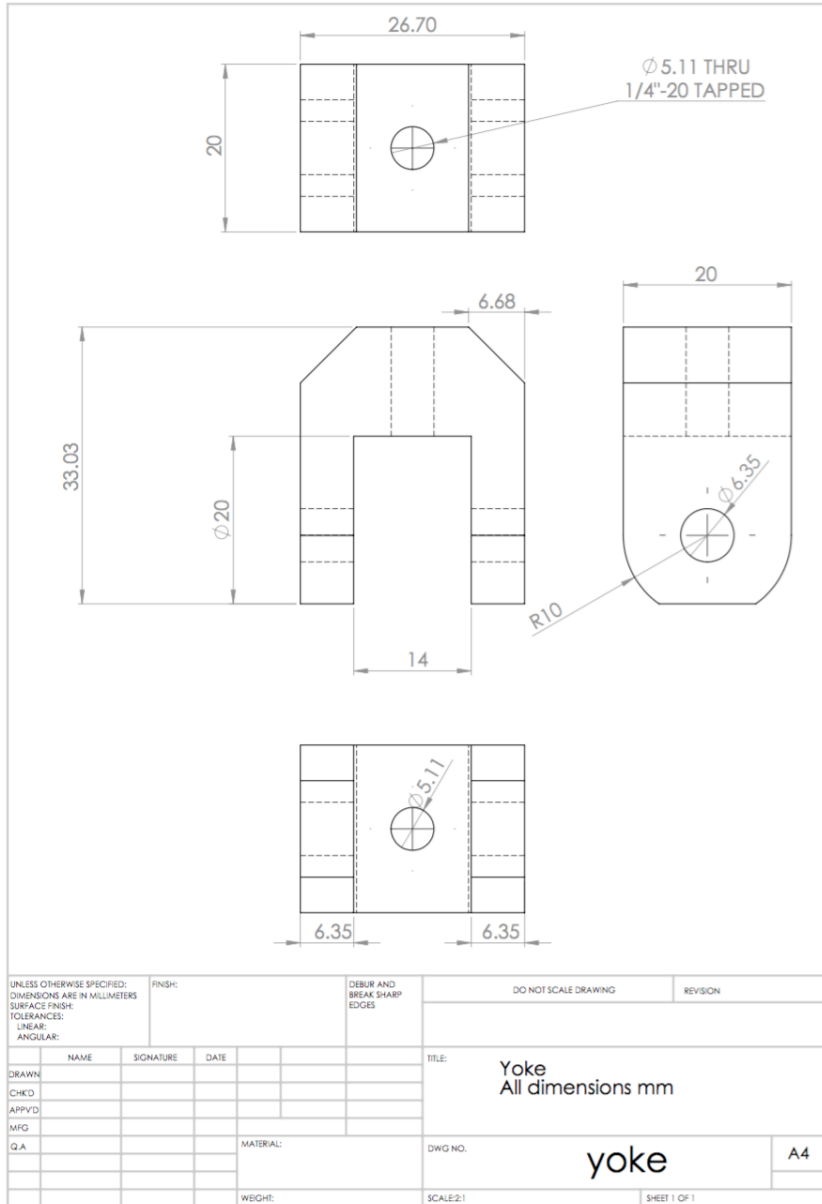
$$y = \frac{a}{1 + b\theta} \left[ \sin(\theta) - \frac{b \cos(\theta)}{1 + b\theta} \right] \quad (9)$$

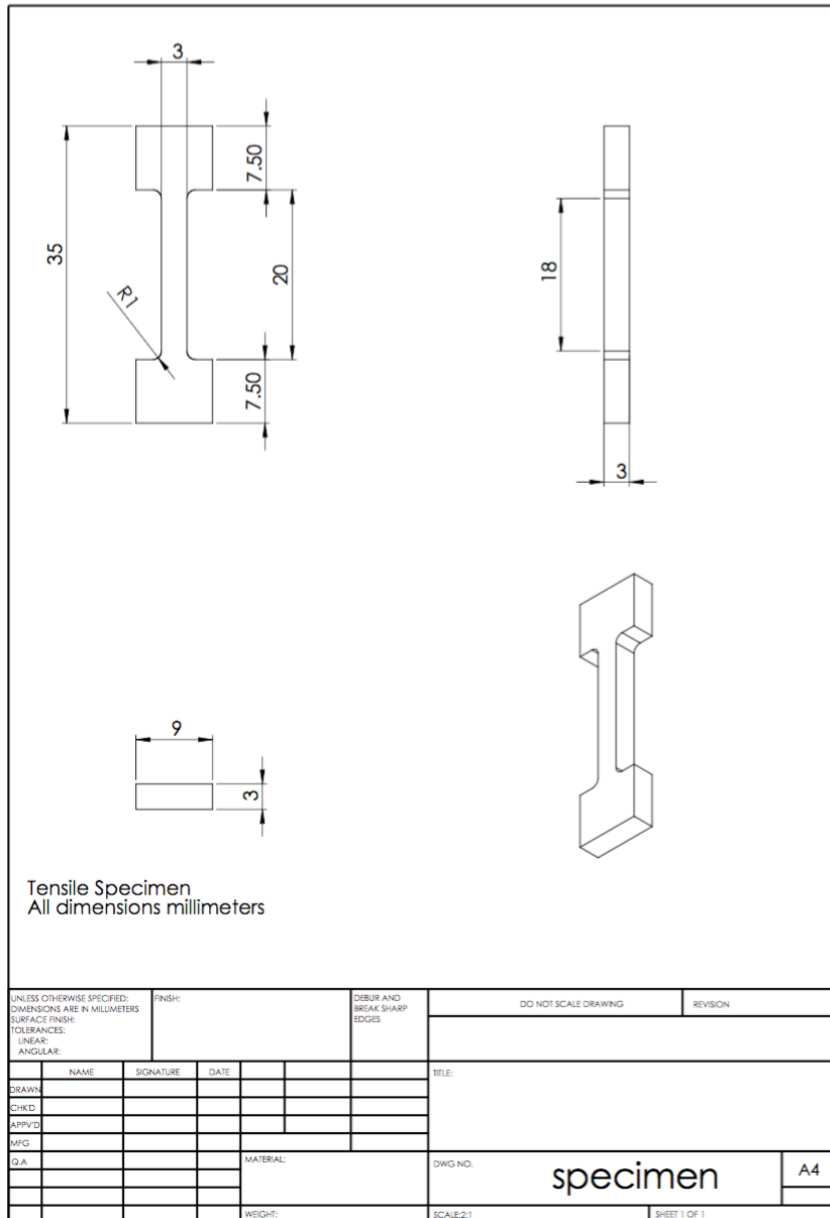
Where:  $a = \frac{r_0 L_0}{L_0 - \pi R_0}$  and  $b = \frac{\pi}{L_0 - \pi R_0}$

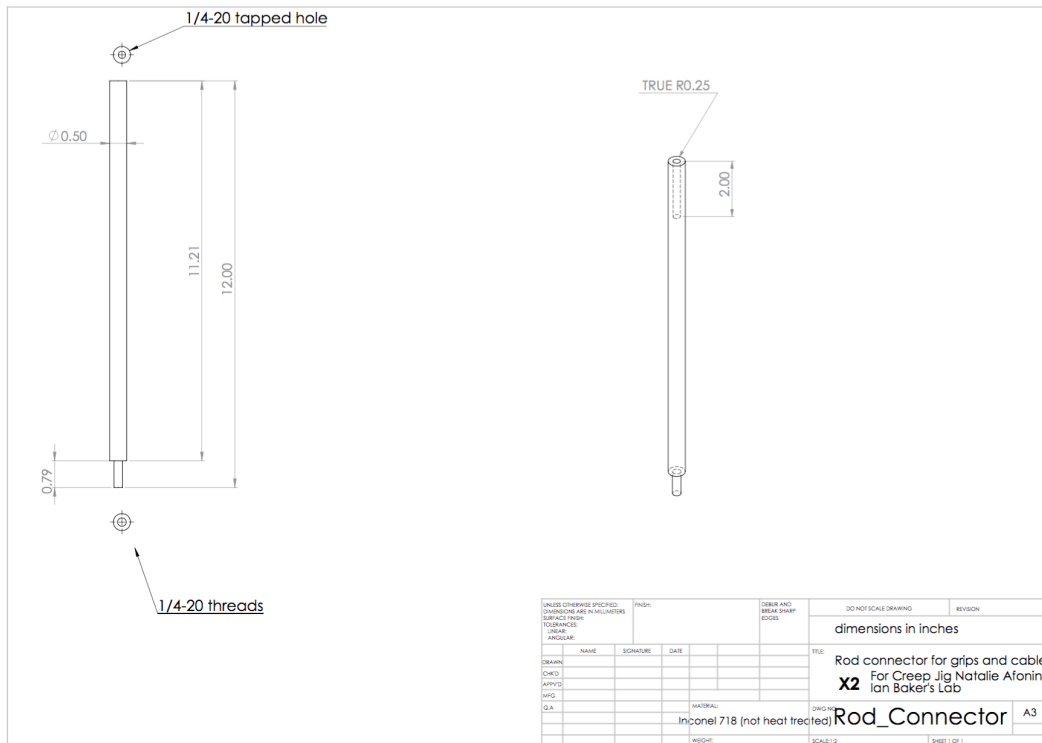
## Appendix II: Custom CAD files for Creep Rig

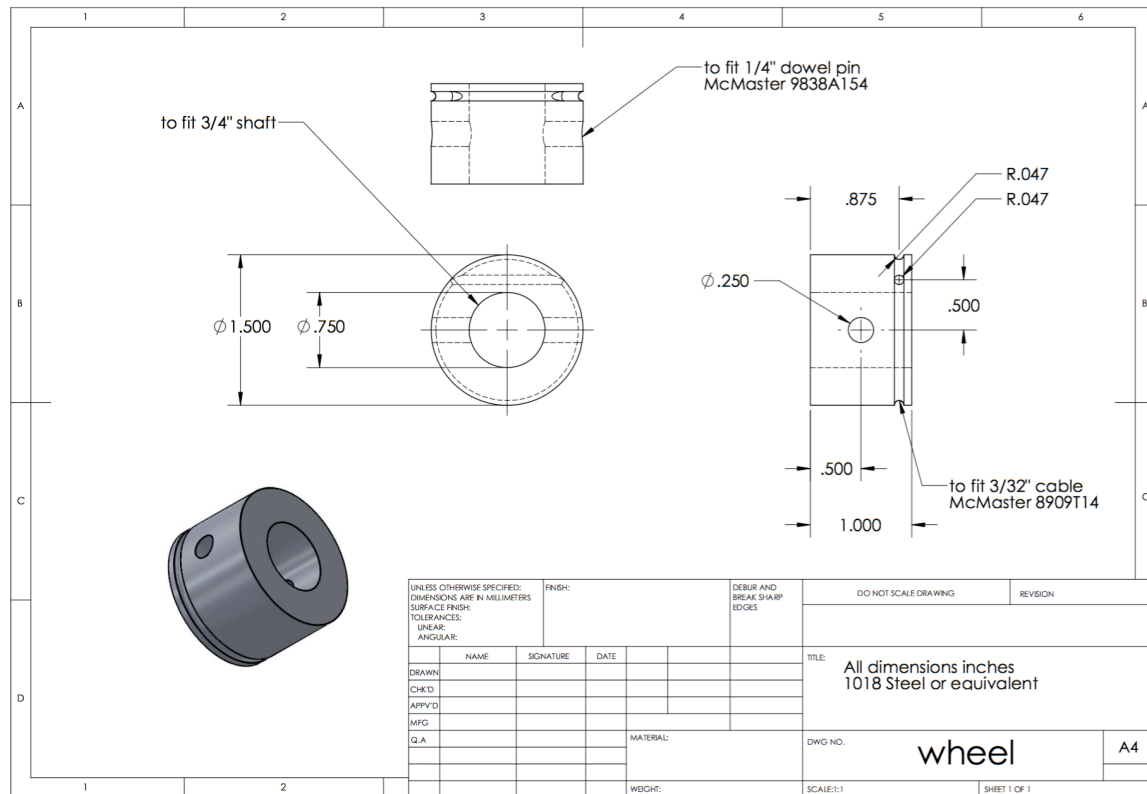


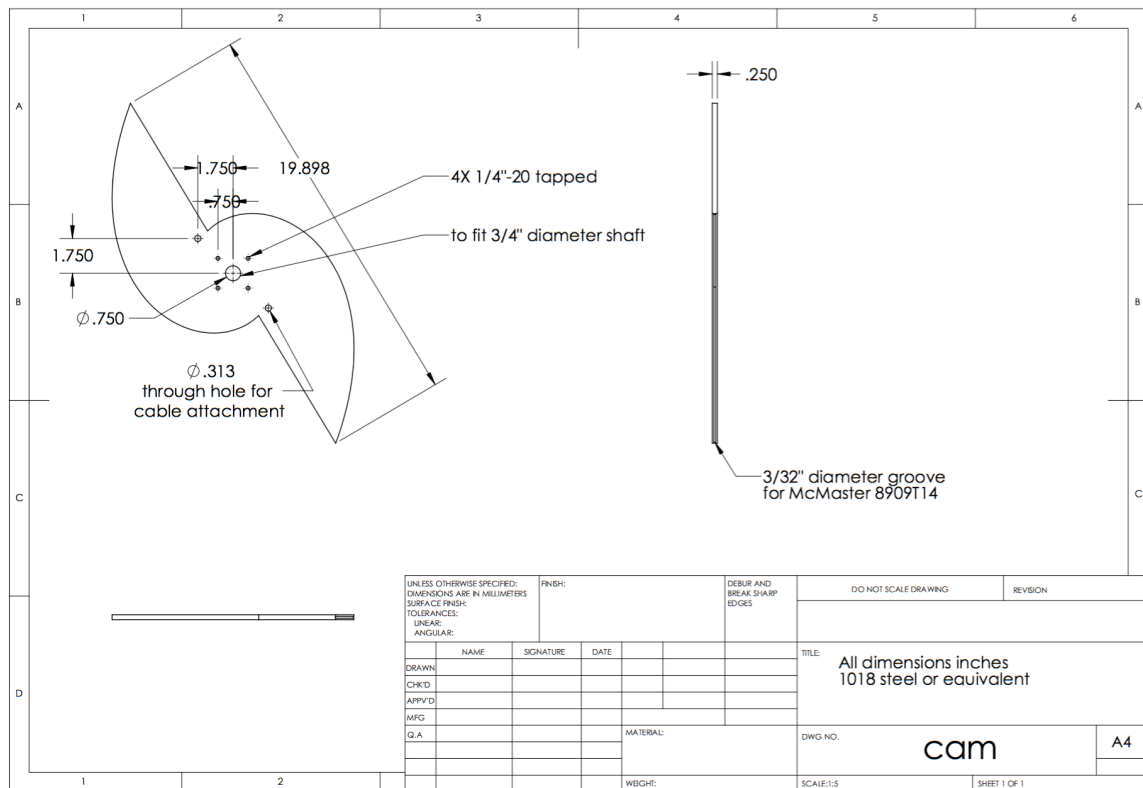




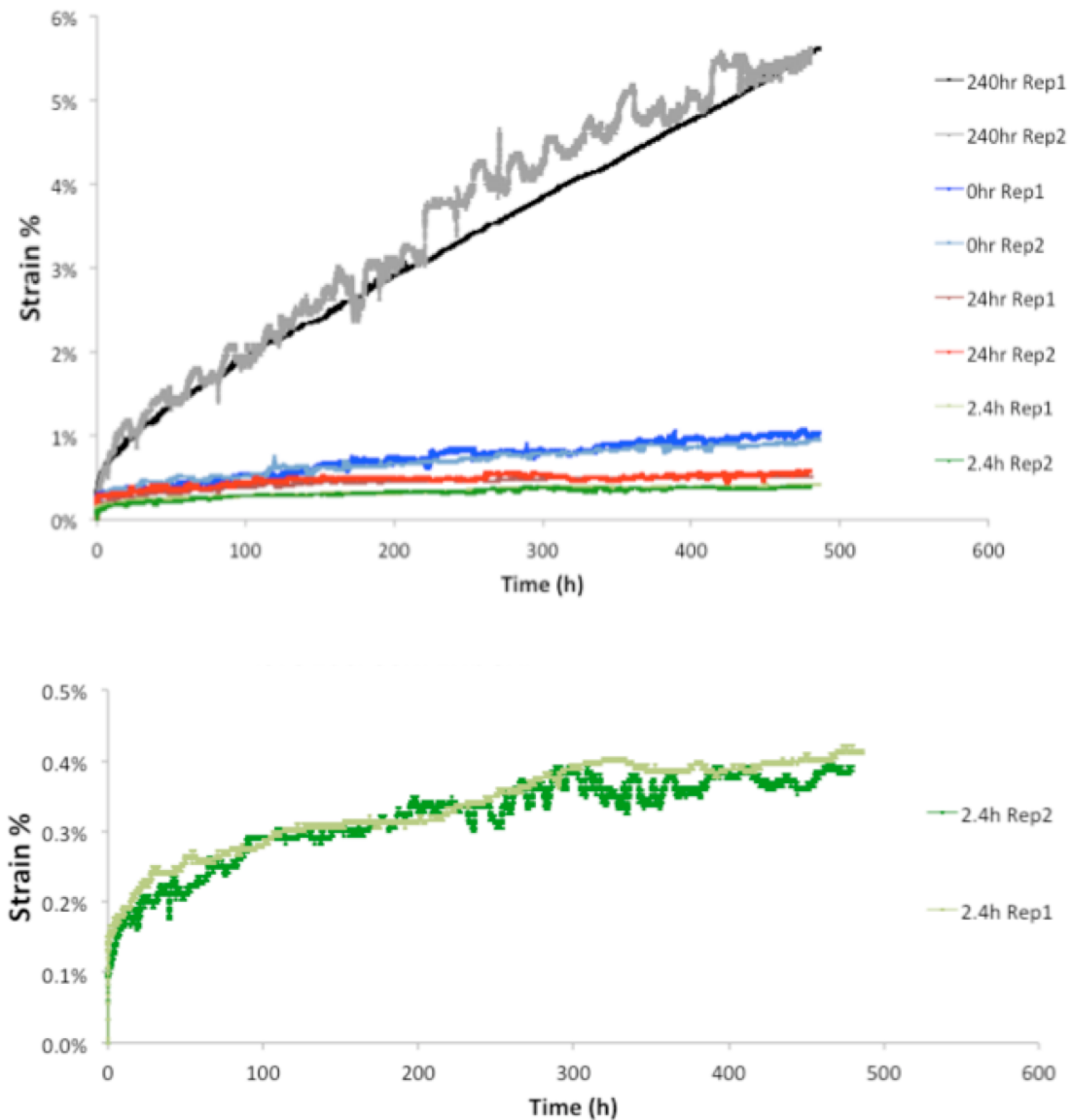


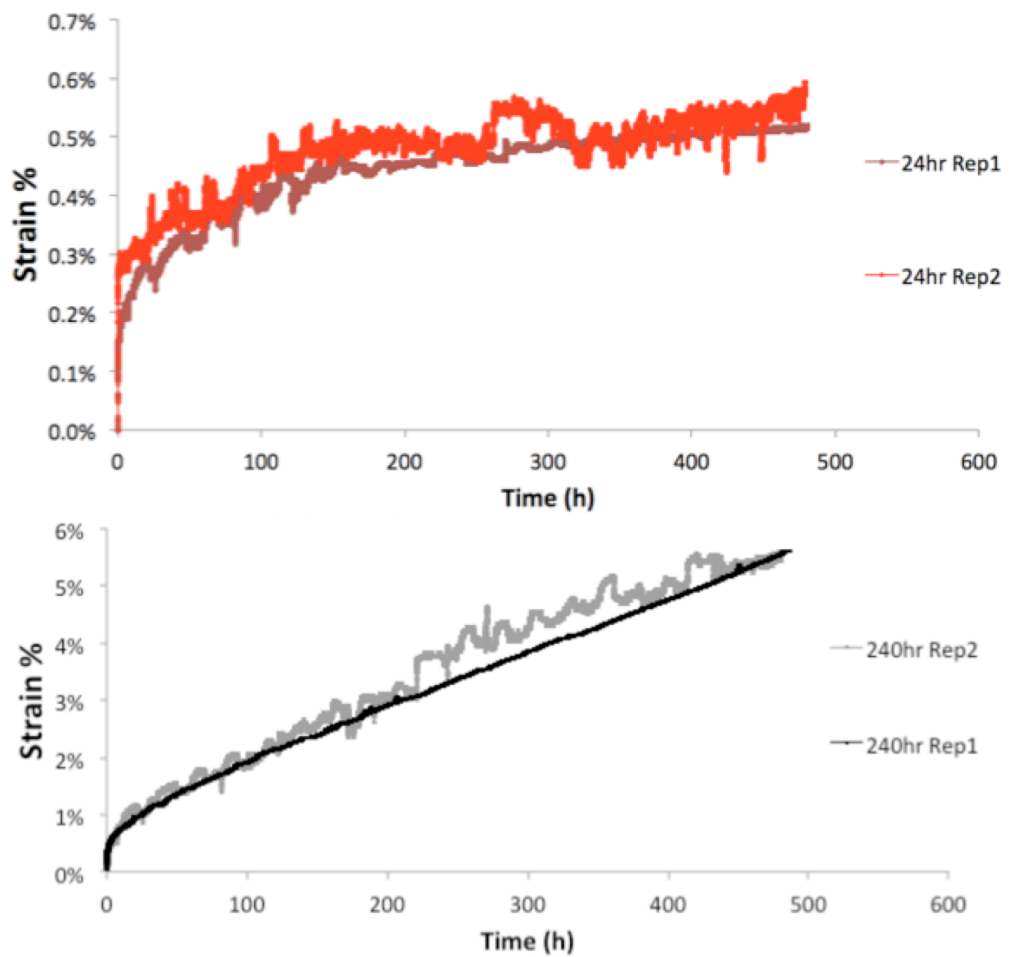
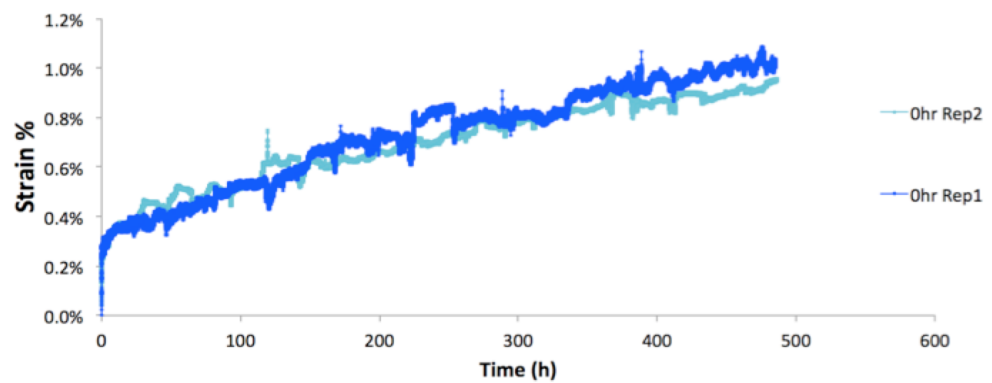




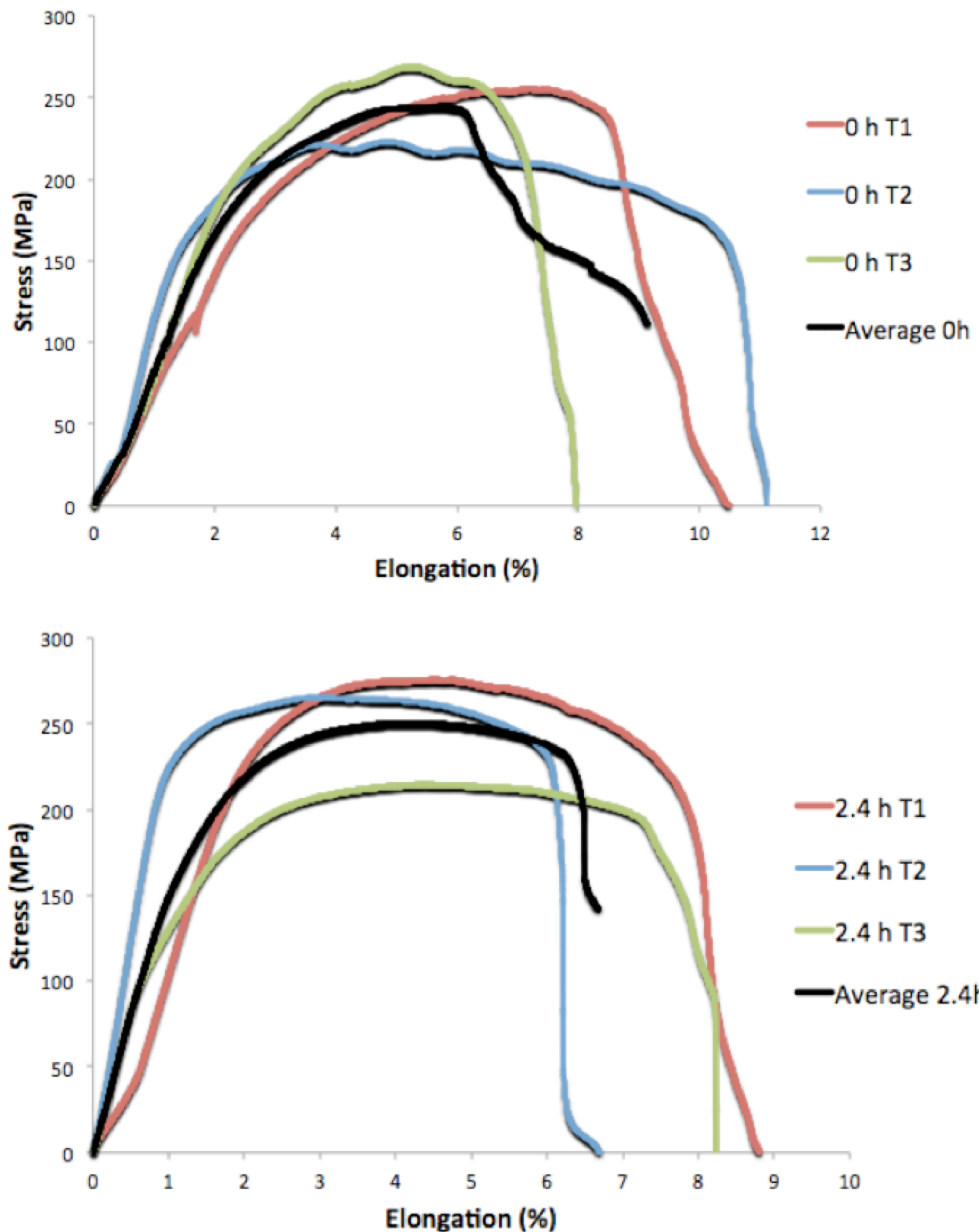


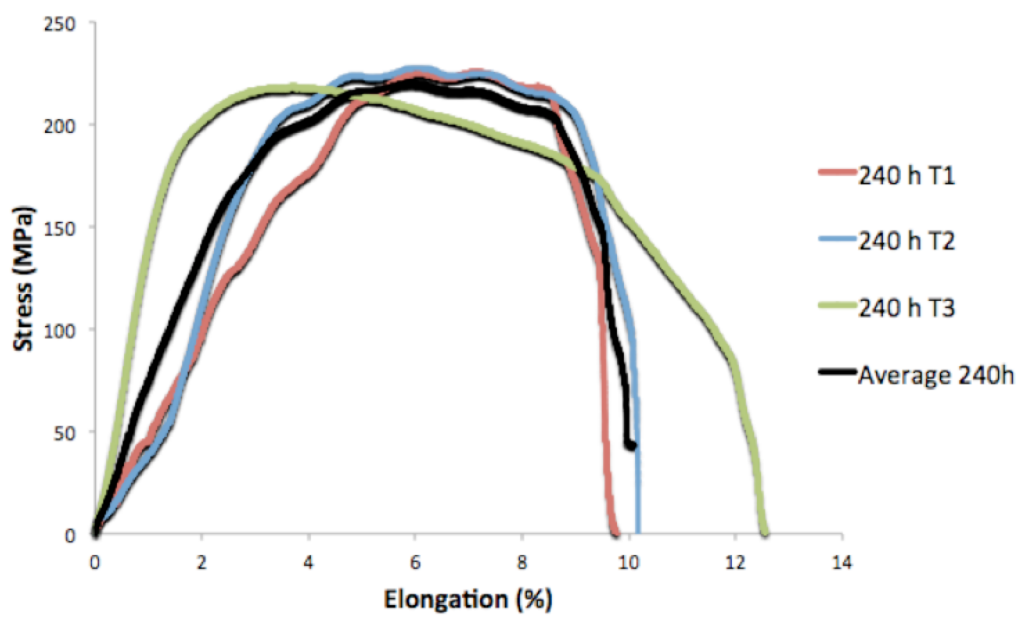
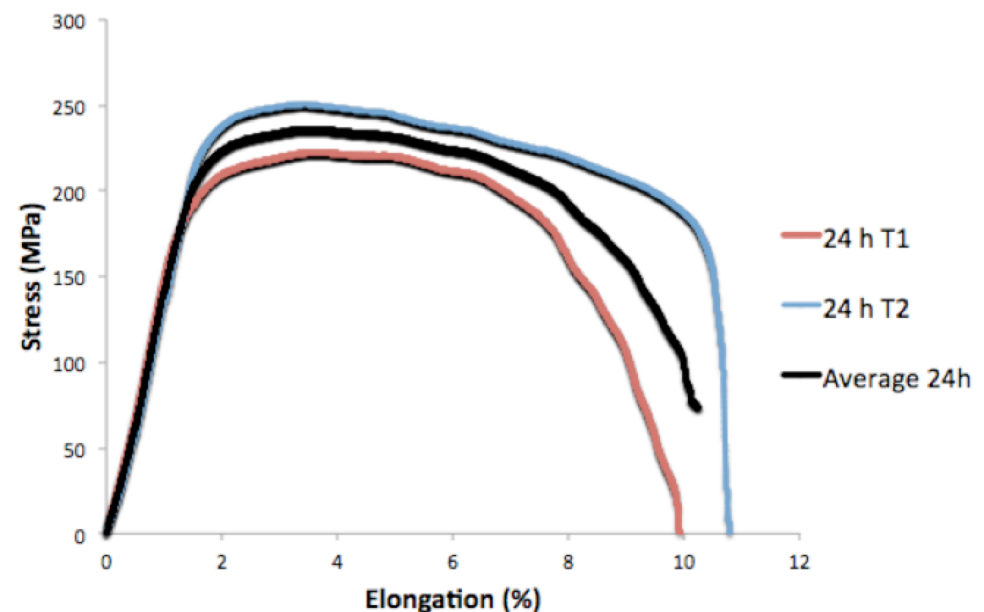
### Appendix III: Additional high temperature constant-stress creep curves for each aging condition





#### Appendix IV: Additional high temperature tensile test curves for each aging condition





## 7 REFERENCES

1. Viswanathan, R., Armor, A. & BOORAS, G. A critical look at supercritical power plants. *Power* **148**, 42–49 (2004).
2. Viswanathan, R., Coleman, K. & Rao, U. Materials for ultra-supercritical coal-fired power plant boilers. *Int. J. Press. Vessels Pip.* **83**, 778–783 (2006).
3. Viswanathan, V., Purgert, R. & Rawls, P. Coal-fired power materials. *Adv Mater Process* **166**, 47–49 (2008).
4. Viswanathan, R. *et al.* US program on materials technology for ultra-supercritical coal power plants. *J. Mater. Eng. Perform.* **14**, 281–292 (2005).
5. Viswanathan, R. & Bakker, W. Materials for ultrasupercritical coal power plants—Boiler materials: Part 1. *J. Mater. Eng. Perform.* **10**, 81–95 (2001).
6. Holcomb, G. R. *et al.* *Ultra Supercritical Turbines--Steam Oxidation*. (Albany Research Center (ARC), 2004).
7. Shingledecker, D. G. and J. *Advances in Materials Technology for Fossil Power Plants: Proceedings from the Seventh International Conference, October 22-25, 2013 Waikoloa, Hawaii, USA*. (ASM International, 2014).
8. Viswanathan, R. *et al.* U.S. program on materials technology for ultra-supercritical coal power plants. *J. Mater. Eng. Perform.* **14**, 281–292
9. Shingledecker, J. P. & Wright, I. G. *Evaluation of the Materials Technology Required for a 760°C Power Steam Boiler*. (Oak Ridge National Laboratory (ORNL), 2006).

10. Yamamoto, Y. *et al.* Creep-resistant, Al<sub>2</sub>O<sub>3</sub>-forming austenitic stainless steels. *Science* **316**, 433–436 (2007).
11. Viswanathan, R. & Bakker, W. Materials for boilers in ultra supercritical power plants. in *Proceedings of 2000 International Joint Power Generation Conference* **20**, (Miami Beach, Florida, 2000).
12. Yamamoto, Y. *et al.* Alumina-Forming Austenitic Stainless Steels Strengthened by Laves Phase and MC Carbide Precipitates. *Metall. Mater. Trans. A* **38**, 2737–2746 (2007).
13. Brady, M. P., Yamamoto, Y., Santella, M. L. & Pint, B. A. Effects of minor alloy additions and oxidation temperature on protective alumina scale formation in creep-resistant austenitic stainless steels. *Scr. Mater.* **57**, 1117–1120 (2007).
14. Brady, M. P. *et al.* The development of alumina-forming austenitic stainless steels for high-temperature structural use. *JOM* **60**, 12–18 (2008).
15. Pint, B. A., Shingledecker, J. P., Brady, M. P. & Maziasz, P. J. Alumina-forming austenitic alloys for advanced recuperators. *ASME Pap. No GT2007-27916* (2007).
16. Brady, M. P., Yamamoto, Y., Santella, M. L. & Walker, L. R. Composition, microstructure, and water vapor effects on internal/external oxidation of alumina-forming austenitic stainless steels. *Oxid. Met.* **72**, 311–333 (2009).
17. Yamamoto, Y., Santella, M. L., Brady, M. P., Bei, H. & Maziasz, P. J. Effect of Alloying Additions on Phase Equilibria and Creep Resistance of Alumina-Forming Austenitic Stainless Steels. *Metall. Mater. Trans. A* **40**, 1868–1880 (2009).

18. Brady, M. P., Magee, J., Yamamoto, Y., Helmick, D. & Wang, L. Co-optimization of wrought alumina-forming austenitic stainless steel composition ranges for high-temperature creep and oxidation/corrosion resistance. *Mater. Sci. Eng. A* **590**, 101–115 (2014).
19. Yamamoto, Y., Muralidharan, G. & Brady, M. P. Development of L1 2-ordered Ni 3 (Al, Ti)-strengthened alumina-forming austenitic stainless steel alloys. *Scr. Mater.* **69**, 816–819 (2013).
20. Yamamoto, Y. *et al.* Alloying effects on creep and oxidation resistance of austenitic stainless steel alloys employing intermetallic precipitates. *Intermetallics* **16**, 453–462 (2008).
21. Yamamoto, Y. *et al.* Overview of strategies for high-temperature creep and oxidation resistance of alumina-forming austenitic stainless steels. *Metall. Mater. Trans. A* **42**, 922–931 (2011).
22. Kofstad, P. & Bredesen, R. High temperature corrosion in SOFC environments. *Solid State Ion.* **52**, 69–75 (1992).
23. Pint, B. A., Distefano, J. R. & Wright, I. G. Oxidation resistance: One barrier to moving beyond Ni-base superalloys. *Mater. Sci. Eng. A* **415**, 255–263 (2006).
24. Pint, B. A., Peraldi, R. & Maziasz, P. J. The use of model alloys to develop corrosion-resistant stainless steels. in *Materials Science Forum* **461**, 815–822 (Trans Tech Publ, 2004).
25. Brady, M. P. *et al.* *Oxidation resistant high creep strength austenitic stainless steel.* (Google Patents, 2010).

26. Yamamoto, Y., Brady, M. P., Lu, Z. P. & Liu, C. Multi-phase high temperature alloys: exploration of laves-strengthened steels. in *Annual Conference On Fossil Energy Materials* 20–27 (Citeseer, 2006).
27. Cahn, J. W. Nucleation on dislocations. *Acta Metall.* **5**, 169–172 (1957).
28. Porter, D. A., Easterling, K. E. & Sherif, M. *Phase Transformations in Metals and Alloys, (Revised Reprint)*. (CRC press, 2009).
29. Chen, S., Zhang, C., Xia, Z., Ishikawa, H. & Yang, Z. Precipitation behavior of Fe 2 Nb Laves phase on grain boundaries in austenitic heat resistant steels. *Mater. Sci. Eng. A* **616**, 183–188 (2014).
30. Pint, B. A. *et al.* Development of alumina-forming austenitic alloys for advanced recuperators. in *ASME Turbo Expo 2009: Power for Land, Sea, and Air* 271–280 (American Society of Mechanical Engineers, 2009).
31. Sourmail, T. Precipitation in creep resistant austenitic stainless steels. *Mater. Sci. Technol.* **17**, 1–14 (2001).
32. Abe, F., Taneike, M. & Sawada, K. Alloy design of creep resistant 9Cr steel using a dispersion of nano-sized carbonitrides. *Int. J. Press. Vessels Pip.* **84**, 3–12 (2007).
33. Stott, F., Wood, G. & Stringer, J. The influence of alloying elements on the development and maintenance of protective scales. *Oxid. Met.* **44**, 113–145 (1995).
34. Reed, R. C. *The Superalloys: Fundamentals and Applications*. (Cambridge University Press, 2008).

35. Trotter, G., Rayner, G., Baker, I. & Munroe, P. R. Accelerated precipitation in the AFA stainless steel Fe–20Cr–30Ni–2Nb–5Al via cold working. *Intermetallics* **53**, 120–128 (2014).
36. Kato, Y., Ito, M., Kato, Y. & Furukimi, O. Effect of Si on Precipitation Behavior of Nb-Laves Phase and Amount of Nb in Solid Solution at Elevated Temperature in High Purity 17% Cr-0.5% Nb Steels. *Mater. Trans.* **51**, 1531–1535 (2010).
37. Liu, C., Zhu, J., Brady, M., McKamey, C. & Pike, L. Physical metallurgy and mechanical properties of transition-metal Laves phase alloys. *Intermetallics* **8**, 1119–1129 (2000).
38. Trotter, G. & Baker, I. The effect of aging on the microstructure and mechanical behavior of the alumina-forming austenitic stainless steel Fe–20Cr–30Ni–2Nb–5Al. *Mater. Sci. Eng. A* **627**, 270–276 (2015).
39. Cao, W. & Kennedy, R. Superalloys 718, 625, 706 and Various Derivatives, ed. EA Loria *TMS* 455–464 (2001).
40. Massalski, T. B., Murray, J. L., Bennett, L. H. & Baker, H. Binary Alloy Phase Diagrams; American Society for Metals: Metals Park, OH, 1986. *There No Corresp. Rec. This Ref.* (1904).
41. Villars, P., Prince, A. & Okamoto, H. *Handbook of ternary alloy phase diagrams*. (Asm Intl, 1995).
42. Tarigan, I., Kurata, K., Takata, N., Matsuo, T. & Takeyama, M. Novel Concept of Creep Strengthening Mechanism using Grain Boundary Fe 2 Nb Laves Phase in Austenitic Heat Resistant Steel. in *MRS Proceedings* **1295**, mrsf10–1295 (Cambridge Univ Press, 2011).

43. Tarigan, I., Takata, N. & Takeyama, M. Grain boundary precipitation strengthening mechanism by Fe<sub>2</sub>Nb Laves phase in creep of Fe-20Cr-30Ni-2Nb austenitic heat resistant steel. in *Proceedings of the 12th International Conference on Creep and Fracture of Engineering Materials and Structure (JIMIS 11)* (2012).
44. Brady, M. P. *et al.* On the loss of protective scale formation in creep-resistant, alumina-forming austenitic stainless steels at 900 C in air. in *Materials Science Forum* **595**, 725–732 (Trans Tech Publ, 2008).
45. Satyanarayana, D., Malakondaiah, G. & Sarma, D. Characterization of the age-hardening behavior of a precipitation-hardenable austenitic steel. *Mater. Charact.* **47**, 61–65 (2001).
46. Satyanarayana, D., Malakondaiah, G. & Sarma, D. Steady state creep behaviour of NiAl hardened austenitic steel. *Mater. Sci. Eng. A* **323**, 119–128 (2002).
47. Garofalo, F., Richmond, O. & Domis, W. F. Design of apparatus for constant-stress or constant-load creep tests. *J. Basic Eng.* **84**, 287–293 (1962).
48. da C. Andrade, E. N. & Chalmers, B. The Resistivity of Polycrystalline Wires in Relation to Plastic Deformation, and the Mechanism of Plastic Flow. *Proc. R. Soc. Lond. Math. Phys. Eng. Sci.* **138**, 348–374 (1932).
49. Kanno, N., Yoshimura, K., Takata, N., Tarigan, I. & Takeyama, M. Mechanical properties of austenitic heat-resistant Fe–20Cr–30Ni–2Nb steel at ambient temperature. *Mater. Sci. Eng. A* **662**, 551–563 (2016).

50. Hu, B. *et al.* The Effects of Cold Work on the Microstructure and Mechanical Properties of Intermetallic Strengthened Alumina-Forming Austenitic Stainless Steels. *Metall. Mater. Trans. A* **46**, 3773–3785 (2015).
51. Yukinori Yamamoto *et al.* Development of Alumina-Forming Austenitic Stainless Steels =Multi-Phase High-Temperature Alloys=. in *Materials Science and Technology Division* (Oak Ridge National Laboratory, 2008).
52. Trotter, G. & Baker, I. Orientation relationships of Laves phase and NiAl particles in an AFA stainless steel. *Philosophical Magazine* **95**, 4078–4094 (2015).
53. Martin, J. W. *Precipitation Hardening: Theory and Applications*. (Butterworth-Heinemann, 2012).
54. Shi, D., Dong, C. & Yang, X. Constitutive modeling and failure mechanisms of anisotropic tensile and creep behaviors of nickel-base directionally solidified superalloy. *Mater. Des.* **45**, 663–673 (2013).
55. Bei, H., Yamamoto, Y., Brady, M. P. & Santella, M. L. Aging effects on the mechanical properties of alumina-forming austenitic stainless steels. *Mater. Sci. Eng. A* **527**, 2079–2086 (2010).
56. Bird, J. E., Mukherjee, A. K. & Dorn, J. E. *Correlations Between High-Temperature Creep Behavior and Structure*. (California Univ., Berkeley. Lawrence Radiation Lab., 1969).
57. Xu, X., Zhang, X., Sun, X. & Lu, Z. P. Effects of silicon additions on the oxide scale formation of an alumina-forming austenitic alloy. *Corrosion Science* **65**, 317–321 (2012).